Geometric Metasurfaces for Ultrathin Optical Devices

Dandan Wen, Fuyong Yue, Wenwei Liu, Shuqi Chen, Xianzhong Chen**

Dr. D. Wen, Dr. F. Yue, Prof. X. Chen
Institute of Photonics and Quantum Sciences, School of Engineering and Physical Sciences, Heriot-Watt University, Edinburgh, EH14 4AS, UK
Email: x.chen@hw.ac.uk

Dr. W. Liu, Prof. S. Chen
The Key Laboratory of Weak Light Nonlinear Photonics Ministry of Education, School of Physics and Teda Institute of Applied Physics, Nankai University, Tianjin 300071, China
The collaborative Innovation Center of Extreme Optics, Shanxi University, Taiyuan, Shanxi 030006, China.
Email: schen@nankai.edu.cn

Metasurfaces, planar metamaterials consisting of a single layer or several layers of artificial structures, not only form the basis for fundamental physics research but also have considerable technological significance. Metasurfaces can locally modify the optical property within a subwavelength range, which can facilitate device miniaturization and system integration. Metasurfaces have shown extraordinary capabilities in the local manipulation of the light's amplitude, phase, and polarization, leading to a plethora of novel applications such as generalized Snell's Law of refraction and photonic spin Hall effect. In this paper, we will focus on the recent advancements in the fundamental research of geometric metasurfaces and their applications in ultrathin optical devices, including planar metalenses, helicity multiplexed holograms, functionality switchable devices, polarization beam splitters, vector beam generation, arbitrary polarization control and so on. The compactness, ease of fabrication and unusual functionalities of these devices render geometric optical metasurface devices very attractive for new applications such as encryption, imaging, anti-counterfeiting, optical communications, quantum science, and fundamental physics. This paper aims to bring readers

some new insights, and to broaden the applications of geometric metasurfaces in more research fields of science and technology.

1. Introduction

When a light beam passes through a transparent material with a certain surface topography, its wavefront will be shaped due to the gradual phase accumulation along the propagation direction, which forms the basis of traditional optical elements design. Due to the limited refractive indices of naturally occurring materials, it is difficult to further reduce the thickness of optical elements based on such a design theory[1]. Metamaterials are artificially structured materials which attain their properties from the unit structures rather than the constituent materials[2], so their optical properties such as the effective electric permittivity and the magnetic permeability can be tuned accordingly [3]. To overcome the fabrication difficulties of metamaterials working in the optical range, a two-dimensional metamaterial, or metasurface has been developed, which consists of a layer of optical antennas to locally modify the phase, amplitude and polarization of the scattered light [1b, 4]. Optical antennas are typically made of metals or high refractive index dielectrics, which can be fabricated through standard nanofabrication process, such as electron beam lithography, lift-off process, focused ion beam milling or reactive ion etching, thus the complexity of the fabrication is greatly reduced in comparison with that for their 3D counterparts. Besides, metasurfaces can change the properties of the scattered light by using antennas with a dimension smaller than the operating wavelength, which exhibits high resolution and can avoid the higher diffraction orders of the traditional diffractive optical devices. In addition, the thickness of the metasurface is much smaller than the incident wavelength which makes them practical for device miniaturization and system integration.

Metasurfaces are generally divided into two categories based on their mechanisms[1a]: the one based on the dispersion of antenna resonance and the one based on the Pancharatnam-Berry phase, namely geometric phase [5]. The former relies on the delicate design of antenna geometry to obtain the desired phase delay of the scattered light. For example, the V-shaped antennas with various arm lengths and opening angles can provide phase gradient to the cross-polarized light, which verifies the generalized laws of reflection and refraction[6]. In contrast, the latter usually contains antennas with the same structure but spatially variant orientations [7]. Each antenna can be regarded as an anisotropic scatterer, which converts part of the incident circularly polarized (CP) light to its opposite helicity with a geometric phase $\pm 2\psi$. The symbol ψ represents the orientation angle of the antenna, with + sign for the conversion from left-handed circularly polarized (LCP) light to right-handed circularly polarized (RCP) light, and the – sign for RCP to LCP light. Thus, a sampled phase function can be imparted to the scattered light from an array of antennas with designed orientations, which are named as geometric metasurfaces [8] and will be focused in this paper.

In this paper, the geometric metasurfaces with different applications will be introduced from Sections 2 to 7. As one of the primary functionalities of metasurfaces, the applications for wavefront control in free space are introduced in Section 2, which is divided into four sections including the lensing, holography, Bessel (Airy) beam generation and helicity-dependent beam steering. In comparison with the extensive wavefront control methods in free space, the methods for surface plasma polariton (SPP) modulation still needs further extension. Here the novel applications of geometric metasurface in SPP control is introduced in Section 3. Like amplitude and phase, polarization is one of the fundamental properties of light. Here in Section 4, optical rotation is realized based on optical metasurfaces, instead of naturally occurring chiral materials or Faraday Effect. A light beam with a helical phase structure is called an optical vortex, which has a dark hole in the center due to the phase singularity of it. This

spinning carries orbital angular momentum (OAM) with the wave train. Benefiting from the flexibility of geometric metasurfaces in wavefront and polarization control, metasurfaces for the generation of twisted light beams and arbitrary manipulation of their superpositions will be discussed in Section 5. Arbitrary polarization generation and its application in image hidden are also covered in this part. Apart from the linear optics, geometric metasurfaces also show great potential for wavefront control and rotational Doppler Effect based on high harmonic generation, which will be introduced in Section 6. Although the majority of metasurface applications fall into the categories shown above, we would like to mention a few other inspiring applications in Section 7. Finally, the conclusion and outlook for future applications will be given in Section 8.

2. Wavefront control in the free space

2.1 Metalens

Traditional lenses focus the incident light through refraction, and their focusing properties are determined by the component materials and the surface topography. In contrast, geometric metasurface-based lens can abruptly change the phase of the scattered light within a deep-subwavelength range, thus greatly reduce the thickness of the lenses. In addition, the unique property of the geometric phase has yielded a series of lenses with unusual functionalities.

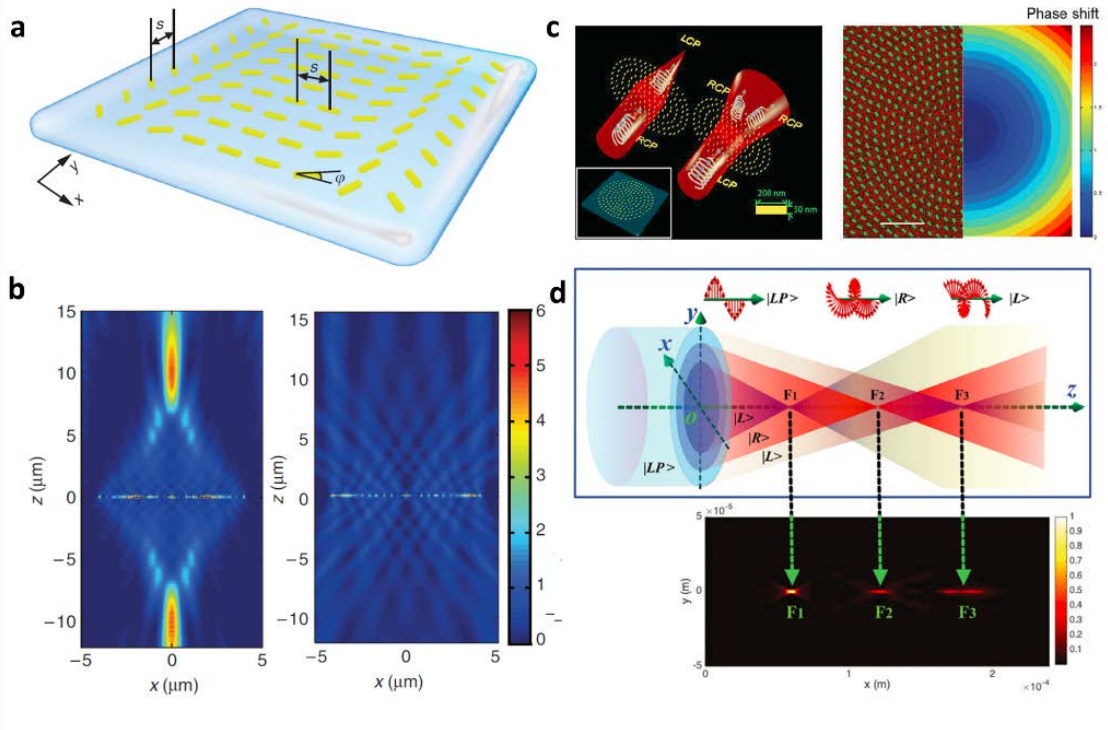

Figure 1. (a) Schematic of the dual-polarity metasurface lens. The orientations of the nanorods gradually change along the *x*-direction, while remain the same in the *y*-direction. The distance *s* between the neighboring nanorods equals to 400nm. (b) The simulation results for the lens under the illumination of the RCP (left) and LCP (right) incident light. (c) Left: schematic of the reversible 3D focusing lens. Right: scanning electron microscopy (SEM) image and phase distribution of the lens. (d) Multi-foci lens that converges the scattered LCP light to points F_1 and F_3, and it also focuses the scattered RCP light to F_2. Figures reproduced with permission from: (a)-(b)[9] Copyright 2012, Nature Publishing Group; (c)[10] Copyright 2013, (d)[11] Copyright 2015, WILEY-VCH Verlag GmbH & Co. KGaA, Weinheim.

As shown in the introduction part, the "+" or "–" sign of the geometric phase is related to the helicity of the incident CP light, which inspires applications that are unachievable by the traditional lenses[12]. **Figure 1**a shows the schematic of a dual-polarity cylindrical lens[9]. For the RCP incident light shining on the metalens, the LCP scattered light in the transmission side forms a bright focal line (figure 1b). However, with the LCP incident light, the RCP scattered

light is diverged and leaves a dim background. The reason lies in the fact that the phase profile of the scattered light is conjugated versus the swap of the incident light helicity. Besides the one-dimensional (1D) focusing by the cylindrical lens, the reversible 3D focusing is realized (figure 1c), and its imaging property is experimentally demonstrated by using the T-shaped aperture array as the target object[10]. If three sublenses with different focal lengths f_1, f_2, and f_3 are integrated, a multi-foci lens can be formed (figure 1d). The sublenses contributing to f_1 and f_3 are designed to work under the LCP incident light, while the sublens corresponding to f_2 works for the RCP incident light. Therefore, the crosstalk between these focal points can be decreased. Such multi-foci lens are claimed to be useful in particle manipulation, imaging, and quantum information processing[11].

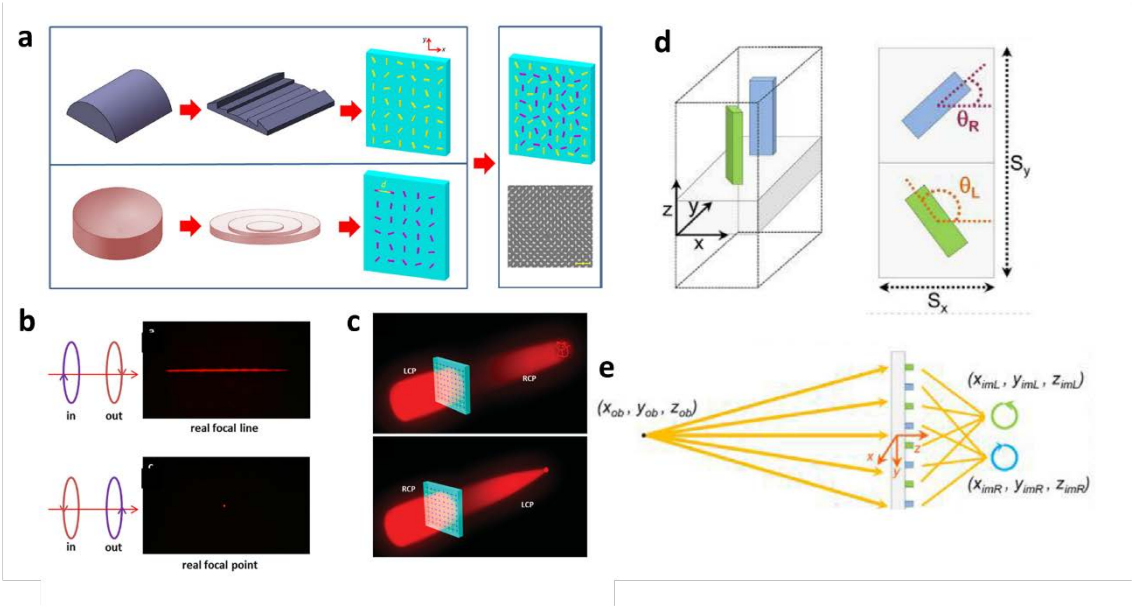

Figure 2. (a) The mechanism schematic of the multifunctional lens. The phase functions of the positive cylindrical lens and the negative spherical lens are encoded on the yellow and purple nanorod arrays, respectively. The merging process only increase the density of the nanoantennas without changing the sample size. (b) The experimental results for the multifunctional lens. (c) The metasurface works as a hologram to form a holographic image of

'cat' for LCP incident light, and it turns into a lens for the RCP incident light. (d) The basic building block of the multispectral chiral lens. The blue and green nanofins contribute to the functionalities required for the RCP and LCP imaging, respectively. (e) Schematics of the chiral lens, where the RCP and LCP light from the target point is focused to two different off-axis points. Figures reproduced with permission from: (a)-(b)[13] Copyright 2016, Nature Publishing Group; (c)[14] Copyright 2015, WILEY-VCH Verlag GmbH & Co. KGaA, Weinheim; (d-e)[15] Copyright 2016, American Chemical Society.

The concept of dual-polarity lens can be further extended to realize a multifunctional lens, which works as a cylindrical (spherical) lens for the RCP (LCP) incident light[13]. Two separate metasurfaces are firstly designed based on the phase functions of the positive cylindrical lens and the negative spherical lens, which are then merged to form the multifunctional lens (**Figure 2**a). Under the RCP incident light, the purple nanorods diverges the scattered LCP light, while the yellow nanorods converges the LCP light to form a bright focal line. Hence the overall performance of the metasurface is a cylindrical lens, and it is easy to infer that the metasurface switches to be a spherical lens for the LCP incident light (figure 2b). The multifunctional metasurface can not only include two phase functions with rigorous mathematical function, but also two arbitrary phase functions as demonstrated in figure 2c[14]. If two arrays of silicon nanofins are interlaced row by row to focus the LCP and RCP light to the corresponding off-axis points, chiral imaging can be realized, where two images with opposite helicity of an object are formed simultaneously[15].

Benefiting from the easy-to-integrate property, metasurface lens fabricated on the stretchable polydimethylsiloxane substrate may have its focal length continuously changed[16]. Alternatively, two metasurface cylindrical lenses are integrated with phase change substrate ($Ge_3Sb_2Te_6$), and each lens selectively interacts with the substrate depending on its amorphous

or crystalline state[17]. Thus, the metalens shows varying focal distance with the temperature which changes the phase of the substrate. In addition to the most frequently demonstrated spherical and cylindrical lenses, the flexibility of the phase control by geometric metasurface also yields a metalens with arbitrary focusing property, such as multiple off-axis focusing[18] and multifocal metalens with conic shapes[19].

The metalenses above unambiguously extend the scope of traditional lenses, however, they still face the problem of high chromatic aberration. Due to the different phase accumulated through propagation with various wavelengths, the position of the focal points changes accordingly although the geometric phase itself is independent of wavelengths. Several methods have been applied to make an achromatic metalens, where focal lengths remain unchanged versus the incident wavelengths. By resorting the principles of holography, the information carried by different wavelengths can be encoded onto a single metasurface, hence achieving an achromatic lens working for λ = 532, 632.8 and 785 nm[20]. The geometric metasurface can also include three different kinds of nanocuboids, which work for the red, green and blue light, respectively. Hence the anticipated wavefront of the three colors can be independently controlled[21]. Geometric phase can also be used in combination with the group phase delay to achieve achromatic property within a broad wavelength range[22].

Besides the novel optical properties of metalenses, the conversion efficiency is the key to their real applications. For the single layer plasmonic metalens, the efficiency is relatively low due to the Ohmic losses and the difficulty of eliminating the zeroth order[23]. It was recently reported that the efficiency can be greatly boosted in the visible wavelength range if the high aspect ratio dielectric nanoantennas are used, e.g. TiO_2 nanofins fabricated on a glass substrate (**Figure 3**a)[24]. Each nanofin behaves as a birefringent antenna where the birefringence is induced by the asymmetric cross section of nanofins. By carefully designing the geometry of the nanofins, the conversion efficiency can reach 86, 73, and 66% at 405, 532, and 660 nm,

respectively. A metalens with high efficiency and numerical aperture (NA) is thus developed that finds application in subwavelength resolution imaging[24-25], spectroscopy[26] and chiral imaging[15]. In addition to TiO_2, the materials for the nanofins can also be GaN (figure 3b)[27] and silicon[28]. Figure 3c shows the metasurface consisting of Si nanobeam array locating on the surface of the SiO_2. The phase difference between the incident TM polarized light and TE polarized light is π at the wavelength of 550nm, so that the beam array functions as a half-wave plate with the fast axis perpendicular to the nanobeams[29]. High efficiency multifunctional metalens with Si nanobeam array are realized to achieve axial and lateral multi-focusing[30]. Besides the pure dielectric metalens, hybrid dielectric–metal metalens consisting of dielectric antennas and the metallic background can be used to achieve high efficiency in the reflection mode for the visible[31] and near-infrared[32] ranges.

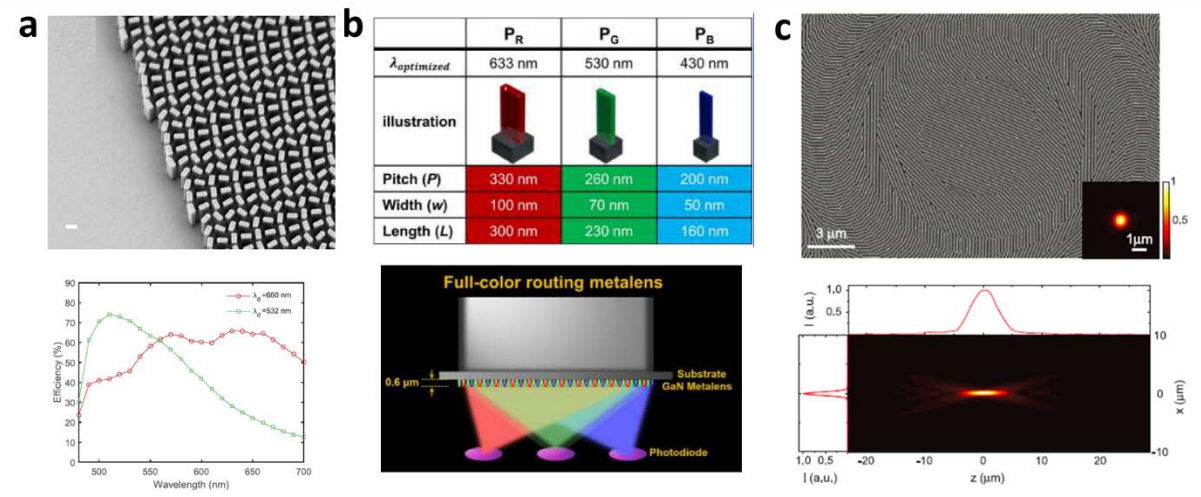

Figure 3. (a) Top: The SEM image of the dielectric metasurface based on TiO_2 nanofins. Bottom: Experimentally measured conversion efficiency of the metalens at 532nm and 660nm. (b) Top: The building blocks of the GaN-based metasurface operating at red, green and blue, respectively. Bottom: Schematic of the color routing metalens that converges and separates the different colors. (c) The SEM image of the metasurface based on Si nanobeam array (top) and the image of its focal point (bottom). Figures reproduced with permission from: (a)[24]

Copyright 2016, (c)[29] Copyright 2014, American Association for the Advancement of Science; (b)[27] Copyright 2017, American Chemical Society.

2.2 Holograms

Computer generated holograms (CGH) can be used to create arbitrary intensity distribution; hence they have numerous applications including particle trapping, optical scanning, virtual reality, and so on. In addition to traditional methods to realize a CGH, such as etching into a dielectric substrate or greyscale lithography, geometric metasurface provides an easier but more efficient way to realize CGHs with incredible performances.

Figure 4a shows a geometric metasurface hologram working in the reflection mode[8]. Each gold nanorod, along with the MgF_2 spacer and the ground reflective layer can be designed to make the whole sandwich-like structure work as a half-wave plate. The peak efficiency reaches 80% at 825 nm, and it also works well within 630 nm to 1,050 nm (figure 4b). To shift the working band to the visible, Si nanoantenna can be used as an alternative, and the image hologram (target image floating just above the sample surface) can be reconstructed even using the natural light[33].

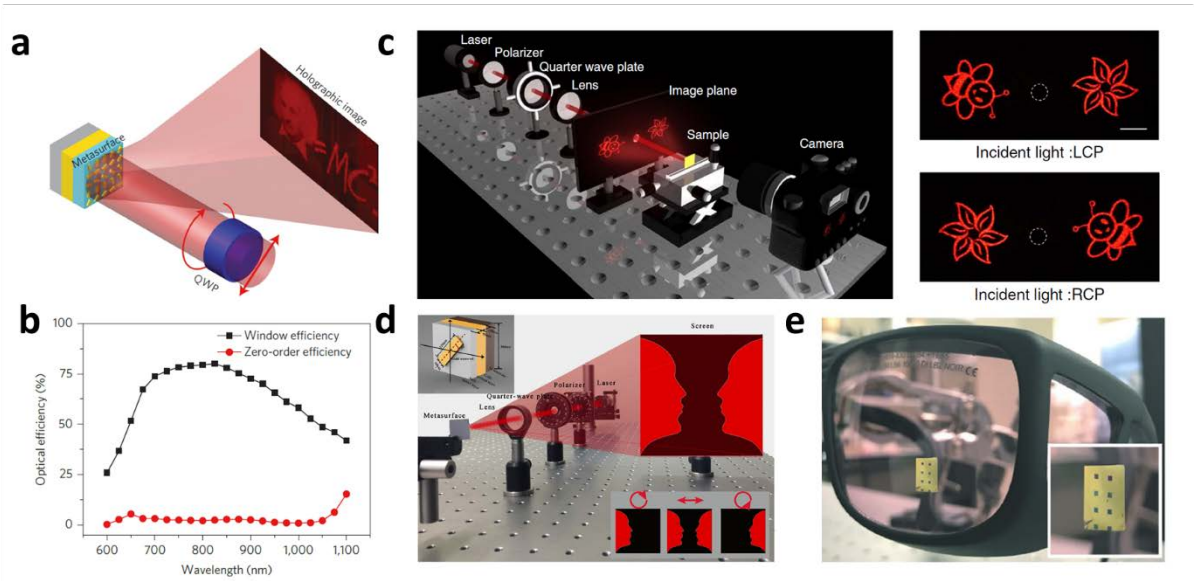

Figure 4. (a) Schematic of the hologram based on the reflective-type metasurface. (b) Measured conversion efficiency of the hologram. (c) Experimental setup for the helicity-multiplexed hologram (left) and the images captured on the screen for the LCP and RCP incident light. (d) Geometric metasurface generated optical illusion. (e) Conformable metasurfaces on a safety glass. Figures reproduced with permission from: (a)-(b)[8] Copyright 2015, (c)[34] Copyright 2015, (d)[35] Copyright 2017, (e)[36] Copyright 2017, Nature Publishing Group.

Although traditional CGHs are generally insensitive to the polarization state of the incident light, a polarization-selective CGH can reconstruct independent holographic images based on the incident polarization state, thereby extending the CGH applications, such as imaging processing and optical switching. Figure 4c shows the operation of a helicity multiplexed hologram[34], where the two images 'bee' and 'flower' swap their positions versus the helicity reversion of the incident CP light. The metasurface can be realized in two different ways: First, two arrays of nanoantennas are integrated to form the metasurface, and each array corresponds to a certain target image 'bee' or 'flower'. Second, a target image includes both 'bee' and 'flower' patterns, each antenna in the metasurface contributes to both patterns. The former method features the flexibility of integrating any two sampled phase functions, while the latter can significantly increase the conversion efficiency. Images of fine quality are achieved in the whole visible wavelength range, and the peak efficiency reaches 59.2% at 860nm. Using the similar principle, two symmetrically distributed "Rubin faces" can be reconstructed on the left and right sides by RCP and LCP light, respectively (figure 4d)[35]. For the linearly polarized incident light, the optical illusion of a 'vase' can be generated. Since helicity multiplexed holograms have great fabrication tolerance, the commonly used silicon substrate can be replaced by soft materials such as SU-8, and the hologram is conformed to a pair of safety glasses[36] (figure 4e).

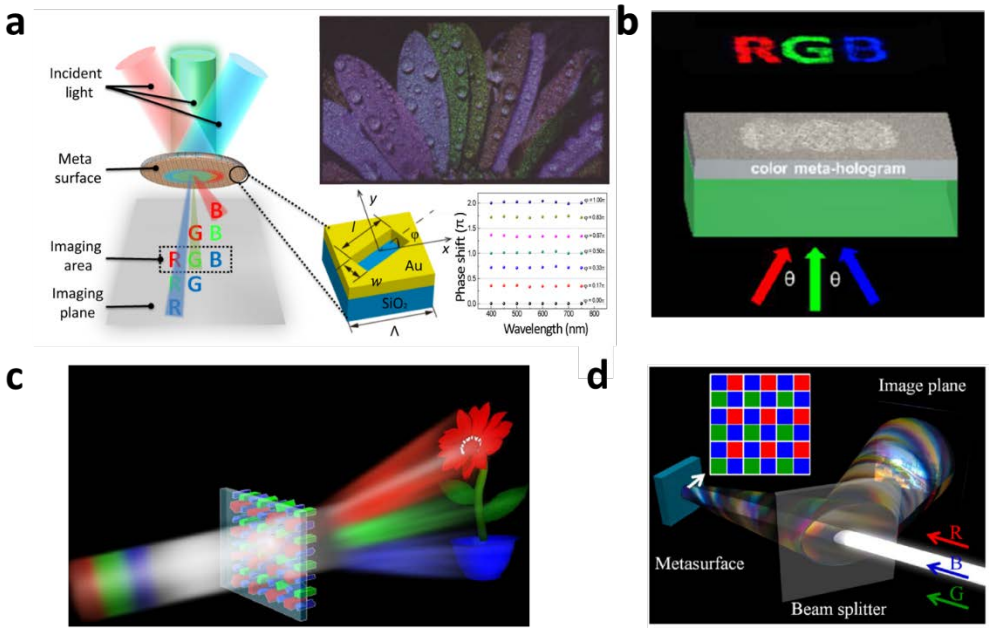

Figure 5. (a) Left: Schematic of the multicolor hologram under the illumination of laser beams with different incident angles. The zoom-in area shows a gold nanoslit antenna. Top right: Experimental results. Bottom right: Simulated geometric phase of the light scattered by an antenna with orientation angle φ. (b) The metasurface consists of aluminum nanoslits. The multicolor image can be reconstructed by the normally incident green light and oblique incident red and blue light. (c) Three kinds of silicon antennas form the metasurface, which can manipulate the R, G, B light independently. (d) Each supercell of the metasurface contains two blue unites, a green unit and a red unit, which only have high efficiency for the corresponding colors. Figures reproduced with permission from: (a)[37] Copyright 2106, American Association for the Advancement of Science; (b)[38] Copyright 2016, (c)[39] Copyright 2016, American Chemical Society; (d)[40] Copyright 2016, The Optical Society of America.

The nature is full of vivid colors, that is why huge effort has been attracted to multicolor holography even as early as in 1960s[41]. Several metasurfaces have been demonstrated to work across the visible spectrum[42], however, further integration of all the RGB components onto a single metasurface must be applied. The schematic of an angular multiplexed multicolor

hologram[37] is shown in **figure 5**a. The target image is first decomposed into the R, G, B components, whose positions are properly arranged to form a new target image. Then the phase distribution is calculated using Gerchberg-Saxton algorithm, and each pixel value is encoded into a nanoslit by controlling its orientation angle. The image with correct colors can be obtained with the off-axis illumination of the red, green and blue laser. The angular multiplexing can also be applied by assigning different phase shifts to the R, G, B parts of the hologram, the corresponding tilted incident light beams can reconstruct the R, G, B image in the designed observation zone[38]. Besides the angular multiplexing method, a more straightforward way is to find out three kinds of nanoantennas that filter out the R, G, B components separately. The R, G, B parts of the hologram can thus be designed independently, and merged together to form a multicolor hologram (figure 5c-d)[39-40, 43].

Geometric metasurface can have subwavelength pixel size and continuous phase levels, which renders them suitable for 3D and multiplane holography. A 3D holographic jet plane with submillimeter size is demonstrated using geometric metasurface consisting of gold nanorods[44]. A 3D object can be regarded as a collection of 2D images subsequently arranged in the longitudinal direction. Therefore as an alternative of 3D holography, multiplane holography reconstructs distinct holographic images at different distances are achieved by using silicon[45] or plasmonic[46] metasurfaces. Usually the multiple images are observed by manually change their distances from the camera. However, if the hologram is fabricated on a stretchable substrate, the stretching can change its pixel size and hence switch the displaced image at a given distance[47]. In addition to the reconstruction distances, multiple images can also be achieved according to the incident light helicity and observation angles, leading to the increase of the information capacity[48].

2.3 Bessel (Airy) beam generation

Bessel beams represent a solution of the Helmholtz equation, and their amplitudes can be described by the first kind Bessel equation. The Bessel beams possess several unique properties such as non-diffraction, self-healing and self-accelerating, which make them suitable for optical tweezing, super-resolution imaging and so on. Traditional ways to generate the Bessel beams usually resort to an axicon or an objective with an annular aperture, however, they have limited NA and additional elements have to be applied for high order Bessel beam generation. Recently, Chen et al. demonstrated a Bessel beam generator with a single dielectric metasurface[49]. The TiO_2 nanofins in the metasurface provide high conversion in the visible range. High NA (0.9) and subwavelength beam size are verified by the experiment. A single catenary aperture in a metallic film can also provide geometric phase from 0 to 2π to the scattered light[50]. Thus, benefiting from the unique phase pattern of a Bessel beam, it can be represented by an array of catenary apertures, which then serves as a Bessel beam generator.

An Airy beam is a non-diffracting waveform that was first theorized in 1979, and it has found applications in partial trapping, laser microfabrication etc. Traditional way for Airy beam generation usually involves the bulky Fourier transform system that hinders the integration. Fan et al proposed a dielectric metasurface Airy beam generator that can precisely control its deflection and focal length[51]. A geometric metasurface can also provide a degree of freedom for controlling the phase and polarization of the Airy beam, thus generating Airy vortex and Airy vector beams[52]. By combining both phase and amplitude manipulation of light parameters, the non-diffracting and self-healing features of Airy beams is also demonstrated[53].

2.4 Helicity-dependent beam steering

Spin-orbital interaction (SOI) refers to the phenomena that the spin affects the intensity distributions and propagation directions of the light beams[54]. The SOI effects can be divided into two categories: internal and external. The internal SOI results from the fundamental

properties of Maxwell equations, such as the split of paraxial beams in inhomogeneous media. The external SOI appears when the light passes through or is reflected by the anisotropic media, such as metasurfaces. Spin-dependent beam splitting by geometric metasurfaces falls into the latter category, and it offers great potential for novel optical applications.

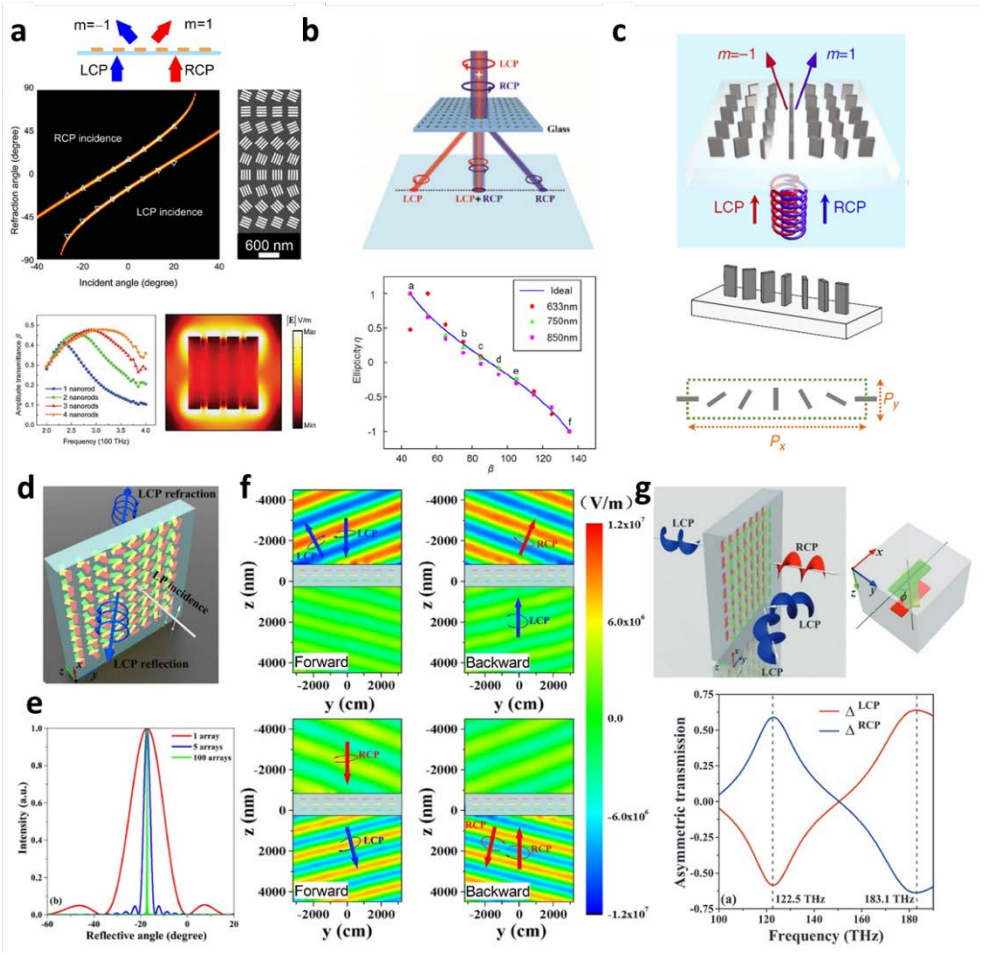

Figure 6. (a) Top: Schematic of the metasurface that deflects LCP and RCP light to different directions. Middle: The deflection angles of LCP and RCP light for different incident angles. Each supercell contains eight nanorods groups with varying orientations. Bottom: By increasing the number of nanorods in each unit cell, the efficiency of the plasmonic metasurfaces increases, and the working waveband expands. (b) Top: The incident light is decomposed partially into the LCP and RCP components, which are anomalously refracted to both sides. Bottom: The ellipticity of the incident light can be deduced by measuring the

intensity of the anomalously refracted LCP and RCP light. (c) Top: The dielectric metasurface deflects LCP and RCP light to different directions. Middle: The metasurface contains amorphous silicon nanofins on a glass substrate. Each supercell contains six nanofins with varying orientations. Bottom: A supercell has the length P_x and width P_y. (d) Schematic of the reciprocal anisotropic few-layer metasurface. (e) The intensity of the reflected light with different number of super cells. (f) Electric field distribution for LCP and RCP light incident from forward and backward directions, respectively. (g) Top: Forward LCP incident light can be converted to RCP transmitted light and backward LCP incident light is reflected to LCP light. Bottom: Calculated asymmetric transmission efficiency for LCP and RCP light. Figures reproduced with permission from: (a)[55] Copyright 2015, g)[56] Copyright 2016, WILEY-VCH Verlag GmbH & Co. KGaA Weinheim; (b)[57] Copyright 2015, The Optical Society of America; (c)[58] Copyright 2014, (d-f)[59] Copyright 2016, Nature Publishing Group

Figure 6a shows the schematic of the metasurface where the orientation of the nanorods group changes periodically along the vertical direction, and they remain the same along the horizontal direction[55]. With the CP incident light, the metasurface provides a phase gradient $d\varphi/dx$ for the converted part, and there is no phase gradient for the unconverted part. It is straightforward to understand that the phase gradient changes to $-d\varphi/dx$ if the helicity of the incident light is reversed. Thus, for the incident linearly or elliptically polarized incident light, the converted LCP and RCP components will be shifted to different directions. The operating efficiency of the metasurface increases with the increasing of the number of the nanorods in each unit cell due to the near field coupling and plasmonic hybridization among the nanorods. The CP light splitting is also achieved through dielectric metasurfaces[58] with a higher conversion efficiency (figure 6c). Similarly, metasurfaces fabricated by the femtosecond laser writing can achieve helicity-dependent beam splitting in the visible range[60]. With careful design of the nanoantenna structures in the beam splitting metasurfaces, nearly 100% conversion efficiency

has been realized in the microwave range[23, 61], and 70% in the near-infrared range[62]. The nanoantennas can even be made of 2D materials such as graphene[63], and the reflectivity is tunable versus the Fermi level E_f. In addition to the nanoantennas with varying orientations, a single slim nanoaperture can also provide phase gradient to the scattered light according to its inclination angle, and hence achieve beam splitting[64]. The metasurfaces mentioned above all shift the LCP and RCP components to different sides. However, if the geometric phase and the propagation phase are both properly controlled, a special spin-dependent splitter can be achieved, which only deflect one polarization component while leaving the other undeflected[65].

In the following, several novel applications have been found based on the unique polarization splitting functionality. Figure 6b shows a polarization measurement method utilizing the phase gradient metasurface[57]. The intensity ratio η_1 between the converted LCP and RCP parts is inversely proportional to the LCP and RCP ratio of the incident light. Hence the intensity distribution of the light spots in the observation plane changes with incident polarization states. The ellipticity and helicity of the incident polarized light can thus be deduced by measuring η_1. Besides the ratio η_1, the intensity difference between the converted LCP and RCP parts denotes the value of Stocks parameter S_3. If the spin-dependent beam splitter is combined with other metasurfaces for measuring S_1 and S_2, the full polarization state of the incident light can be obtained[66].

The metasurfaces with large phase gradient can not only divert the LCP and RCP components, but they are highly dispersive, i.e. different wavelength can be separated with high resolution. Hence the spectrum for the LCP and RCP components of the incident light can be obtained simultaneously[67]. The polarization beam splitting can happen along any phase-gradient direction, including both the transverse and longitudinal directions. By integrating the phase gradients along the two directions with a dynamic phase lens, the scattered LCP and RCP parts

are not only separated, but also focused to different positions[68]. Spin-dependent splitting and focusing are also realized in the THz range, where the phase gradients along both directions are achieved by the distribution of the antennas[69]. Since the LCP and RCP images of the target object can be simultaneously formed, interesting functionalities such as the circular dichroism measurement can be performed with a simplified imaging system.

As mentioned above, the efficiency of dielectric metasurfaces are usually higher than plasmonic metasurfaces due to the abundant resonances of dielectric nanoantennas, such as waveguide modes, simultaneous electric and magnetic dipole resonances. One way to significantly increase the efficiency of the plasmonic metasurfaces is to increase the effective interaction distance of light travelling in nanoantennas. In recent years, Cheng et al. proposed few-layer metasurfaces that can remarkably expand the functionalities of plasmonic metasurfaces with high efficiency[70]. These few-layer metasurfaces can generate near field interaction[71], Fabry-Pérot resonances[72], waveguide modes[73] between layers, leading to expansion of functionalities and improvement of efficiency. As shown in figure 6d-f, a three-layer geometric metasurface is proposed to generate high-efficiency asymmetric anomalous refracted and reflected light[59]. The orientation of nanorods in each unit cell is different from each other, which leads to a multi-wave interaction to increase the effective propagation distance in the metasurface. When the LCP and RCP light is incident from forwards and backwards, the metasurface plays different roles of spin conversion and spin reflection. This effect can also be utilized to achieve asymmetric transmission (figure 6g), and the asymmetric transmission coefficient reaches 0.638 at 183.1 THz[56]. This designing methodology can also extend to acoustic metasurfaces to achieve feasible coding acoustic metasurface[74] and asymmetric transmission[75].

Furthermore, the strength of the CP light can be modulated by simultaneous incident LCP and RCP light[45, 76]. With accurate control of the incident angles and relative phase of the CP light,

the intensity of the refracted anomalous light can be dynamically tuned (**figure 7**a-b). This phenomenon originates from the interference of the anomalous and ordinary refracted light, which is highly dependent on the incident angle and relative phase of the CP light. Similar method has been adopted in linearly polarized incident light to control the intensity of the refracted light by changing the incident polarization direction[77]. The helicity-dependent beam steering is also realized through graphene based metasurfaces. Graphene, 2D material with high carrier mobility, is capable of generating plasmonic resonances[78]. Cheng et al. proposed graphene nanocrosses to achieve broadband optical beam steering in the infrared waveband[79], as shown in figure 7c-d. The efficiency of such metasurfaces is near to that of metallic plasmonic metasurfaces. One of the advantages of employing graphene is that the intensity of the refracted light dynamically changes with the Fermi level of graphene. Since the graphene nanostructure with size decreasing to $\lambda/80$ still can generate plasmonic resonances, the graphene based metasurfaces working in deep sub-wavelength scale are capable of realizing high-order optical modulation such as high-order diffraction (figure 7e) and high-order optical vector beams[80].

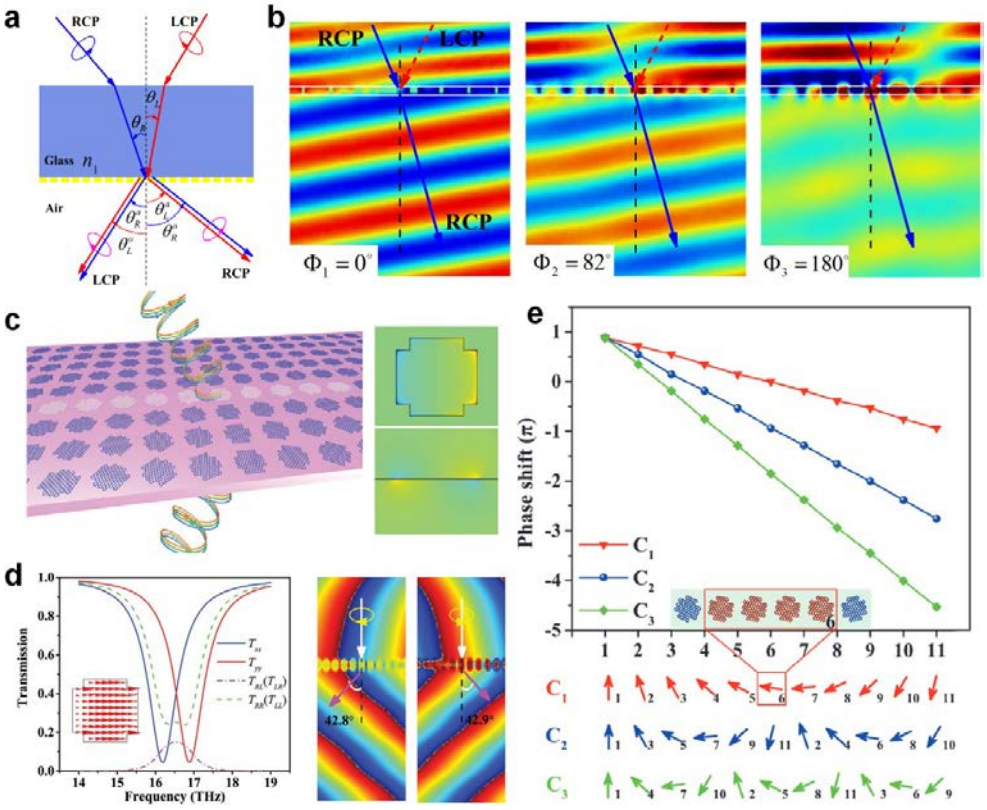

Figure 7. (a) The strength of the anomalous refracted light can be dynamically controlled by simultaneous LCP and RCP incident light. (b) The electric distribution of the refracted RCP light with different relative phase Φ of 0°, 82°, 180°, respectively. (c) Schematic of the graphene based geometric metasurface and the near field electric distribution. (d) Transmission spectra of the graphene nanostructure under linear polarized and CP light. The LCP and RCP light propagate to different directions when passing the metasurface. (e) Phase shift of different graphene groups to achieve high-order anomalous reflection. The graphene nanoantenna is similar to that in (c-d) with reduced size. Figures reproduced with permission from: (a-b)[76] Copyright 2014, The Optical Society of America; (c-d)[79] Copyright 2015, (e)[80] Copyright 2018, WILEY-VCH Verlag GmbH & Co. KGaA Weinheim.

3. Wavefront shaping of SPP

In addition to the wavefront control in the free space, geometric metasurfaces can serve as bridges to link the SPP waves with the incident light, hence shaping the SPP wavefront. Novel

applications can be found such as SPP directional coupling and helicity-dependent wavefront control, which dramatically improves the near-field applications of SPPs.

Despite different mechanisms have been applied for SPP launching, such as the prism coupling and grating coupling, the excited SPP waves always have the fixed propagation direction. By utilizing the helicity-dependent phase gradient generated by the geometric metasurface, the SPP unidirectional excitation can be realized[81]. When the incident light changes from RCP to LCP, the phase matching condition is shifted, and the direction of the SPP excitation (**figure 8**a). With the LCP or RCP incident light, the excited SPP shows high extinction. However, SPPs along both directions can be excited with elliptically or linearly polarized incident light, which offers another freedom for SPP control[81a].

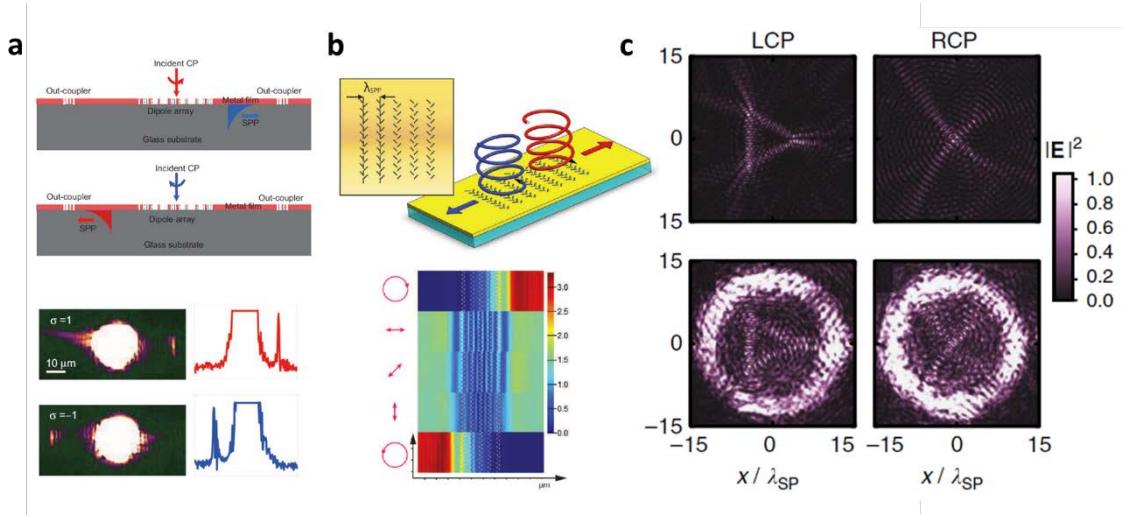

Figure 8. (a) Schematic (top) and experimental results (bottom) of the unidirectional SPPs excitation. With the RCP(LCP) incident light, the SPP travels to the right(left) side and coupled out by the coupler. (b) Top: The parallel nanoslit pairs are repeated to form the metasurface, which couples the incident light to different directions according to its helicity. Bottom: Simulation results for the near-field distribution under different incident polarization states. (c) Top: Simulated (top) and experimentally obtained (bottom) SPP profiles for the LCP and RCP incident light. Figures reproduced with permission from: (a)[81a] Copyright 2013, (c)[82]

Copyright 2015, Nature Publishing Group; (b)[83] Copyright 2013, American Association for the Advancement of Science.

The directional scattering of the SPP can also be realized in another way, where each nanoaperture defined in the metallic film can be regarded as a dipole that scatters the incident light polarized perpendicular to its long axis[83]. Under the illumination of CP light, the phase of the scattered SPP wave change with the orientations of the nanoslits[84]. Hence two columns of nanoslits with perpendicular orientations and a properly designed spacing can serve as the spin-dependent directional coupler (figure 8b). The nanoslits can be replaced by nanorods placing on top a graphene layer to directionally excite the graphene plasmons[85].

It is interesting to note that nanoslit arrays arranged in a ring[83] or spiral shape[86] can form a helicity-dependent plasmonic lens. Under the matched CP light, the SPP will be focused into the central point, or else it will be diverted for the orthogonal polarization. Thus, the lens is used as a plasmonic CP light analyzer[85, 87]. The spiral shaped nanoslits array can also be used to control the OAM of the SPPs by simultaneously utilizing the geometric phase and the dynamic phase[88].

Similar to the principles of the CGHs, the desired SPP wave profile can serve as the target image and the geometric metasurface acts as a holographic coupler. By using a geometric phase matching scheme i.e. the method to deduce the angles of the nanoslits array from the target pattern, two SPP beams generated by LCP and RCP light can cooperate with each other, and reconstruct helicity-dependent SPP profiles (figure 8c)[82, 89].

4. Optical rotation

Light with linear polarization has equal LCP and RCP components, and if the light passes through certain material with circular birefringence, i.e. the refractive indices for the LCP and

RCP light are different, the polarization angle of the output light will be rotated. This phenomenon has given birth to many useful applications, such as concentration determination[90] and organic structure analysis[91]. Traditional way to obtain optical rotation usually resorts to chiral materials or Faraday effect, but it is difficult to minimize such devices due to the weak rotation coefficient in the naturally available materials. By mimicking the natural chiral materials, 3D chiral metamaterials can effectively manipulate the polarization rotation[92], but it suffers from fabrication difficulties. Chiral metasurfaces are also developed[93], however, the magnitude of the rotation angle is limited. In comparison, geometric metasurfaces can realize optical rotation without resorting to the chiral antennas, and the major approaches will be introduced in this section.

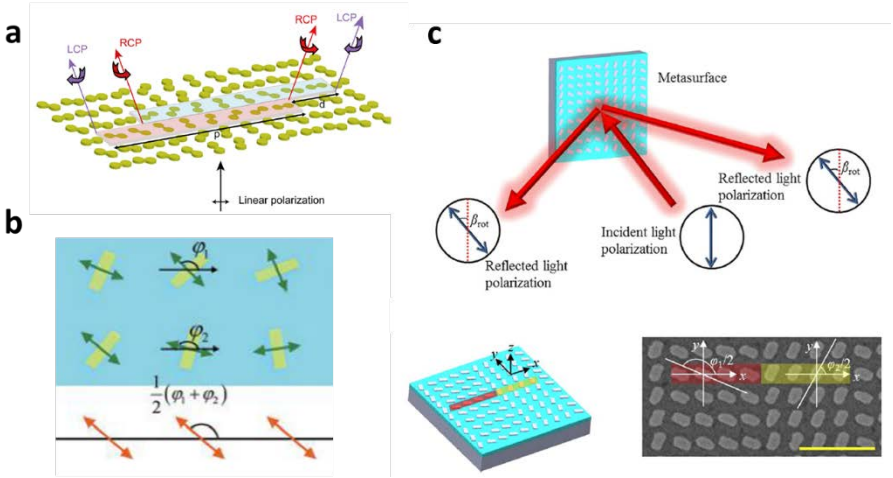

Figure 9. (a) Schematic of the metasurface for optical rotation. It contains two kinds of subunits, with an offset distance *d*. (b) A single unit of the metasurface half-wave plate is composed of two antennas with orientation angles φ_1 and φ_2, the optical axis has the direction $(\varphi_1 + \varphi_2)/2$. (c) Top: The optical rotation process: an incident light beam is rotated by angle β_{rot} after reflection. Bottom left: Schematic of the metasurface. Bottom right: SEM image of the metasurface. Figures reproduced with permission from: (a)[94] Copyright 2014, (b)[95] Copyright 2017, American Chemical Society; (c)[96] Copyright 2017, American Institute of Physics.

For geometric metasurfaces, the optical rotation of the output beam can be obtained by the collective function of all the antennas. As shown in **figure 9**a, the metasurface contains two subunits, both of which can decompose the incident light to LCP and RCP components, and send them to different directions[94]. With the displacement of the two subunits, the phase difference $\Delta\Phi$ is provided to the co-propagated LCP and RCP light, which then recombine and form a new polarization state. Since the rotation angle equals to $\pi d/p$, it is convenient to control the optical rotation angle through the arrangement of the subunits. To boost the conversion efficiency , reflective-type metasurface can be used[97] and multiple beams with different polarizations are generated simultaneously[98]. Since the optical rotation is only obtained through the geometric phase, it can even rotate a vector field regardless of its nonuniform spatial polarization distribution[99].

For a traditional half-wave plate, optical rotation can be achieved due to the different phase accumulation along its fast and slow axes. Similarly, Liu et al. developed a metasurface half-wave plate, where a subunit is composed of two nanorods with the orientation angles φ_1 and φ_2 (figure 9b)[95]. For the linearly polarized incident light with the polarization direction φ, the output light will be rotated to $\varphi_1+\varphi_2-2\varphi$. As shown in figure 9c, a metasurface-based rectangular phase grating is demonstrated for optical rotation. There are only two subunits, with the orientation angles of $\varphi_1/2$ and $\varphi_2/2$. The linearly polarized incident light can be decomposed into the RCP and LCP components, and their phase difference $\Delta\varphi$ is related to φ_1 and φ_1, thus the rotation angle can be easily controlled with properly designed $\Delta\varphi$ [96].

5. Orbital angular momentum and vector beam generation

There are two kinds of angular momenta that a light beam can carry: the spin angular momentum (SAM) and the orbital angular momentum (OAM). SAM can only have two values, $\pm\hbar$ per photon, corresponding to the LCP and RCP light, respectively. While OAM can have

the values of $l\hbar$ per photon, $l = 0, \pm 1, \pm 2, \pm 3.....$. **Figure 10**a shows sample examples of OAM beams with different topological charges. A topological charge refers to the number of the twist in one wavelength or the number of azimuthal phase windings about the beam axis. The higher the topological charge, the faster the light is spinning around its axis. The wavefront, the phase distribution, and the intensity profile are presented in this figure.

Despite many approaches and methods[100] have been proposed to generate the OAM beams, these systems are typically bulky in size, which hinders their applications in integrated optics. Moreover, the limited resolution of the spatial light modulators, low damage threshold of the *q*-plates still need to be overcame for practical applications. The progress in nanofabrication techniques has enabled the development of metasurfaces to control the wavefront of the incident light in the subwavelength domain. By spatially adjusting the geometric parameters of unit cell of metasurface, one can generate and control the OAM at will[101]. For instance, a plasmonic metasurface is demonstrated to impart the OAMs to the incident CP plane waves[101b] (figure 10b). A three-dimensional volumetric optical vortices generator is realized using geometric metasurface with dielectric nanopatterns[102]. The concepts of Dammann vortex gratings and spiral Dammann zone plates were employed to generate vortex arrays (figure 10c). Not only can metasurface be utilized to generate the OAM states, it also provides a flexible way to manipulate the superposition of two OAM states. Yue *et al*. proposed and demonstrated a metasurface approach to realize polarization-controllable multichannel superpositions of OAM states with various topological charges[103]. Under the RCP incident light, four OAM states ($\text{from} l = 1 \text{to} l = 4$) are generated at the same time (figures 10d, e). By manipulating the polarization state of the incident light, different OAM superpositions are realized in different channels. As in figure 10d, if the incident light changes to be linearly or elliptically polarized, the left channel will be the superpositions of $l = 3$ (RCP) and $l = -1$ (LCP), and the right channel corresponds to the $l = 1$ (RCP) and $l = -3$ (LCP). It is similar for the top and bottom

channels, and the case for the right channel under different incident polarization states is shown in figure 10f. Later, a method for imparting independent OAMs to two orthogonal polarizations was proposed[104] (figures 10g, h). Owing to its capabilities of arbitrary engineering of phase at nanoscale, metasurface shows great potential in system integration and device miniaturization. For example, Zhang *et al*. showed a metasurface device with tunable functionalities including polarization-controllable hologram generation and superposition of orbital angular momentums[105]. Figure 10i shows the experimental results of holograms and vortex beams.

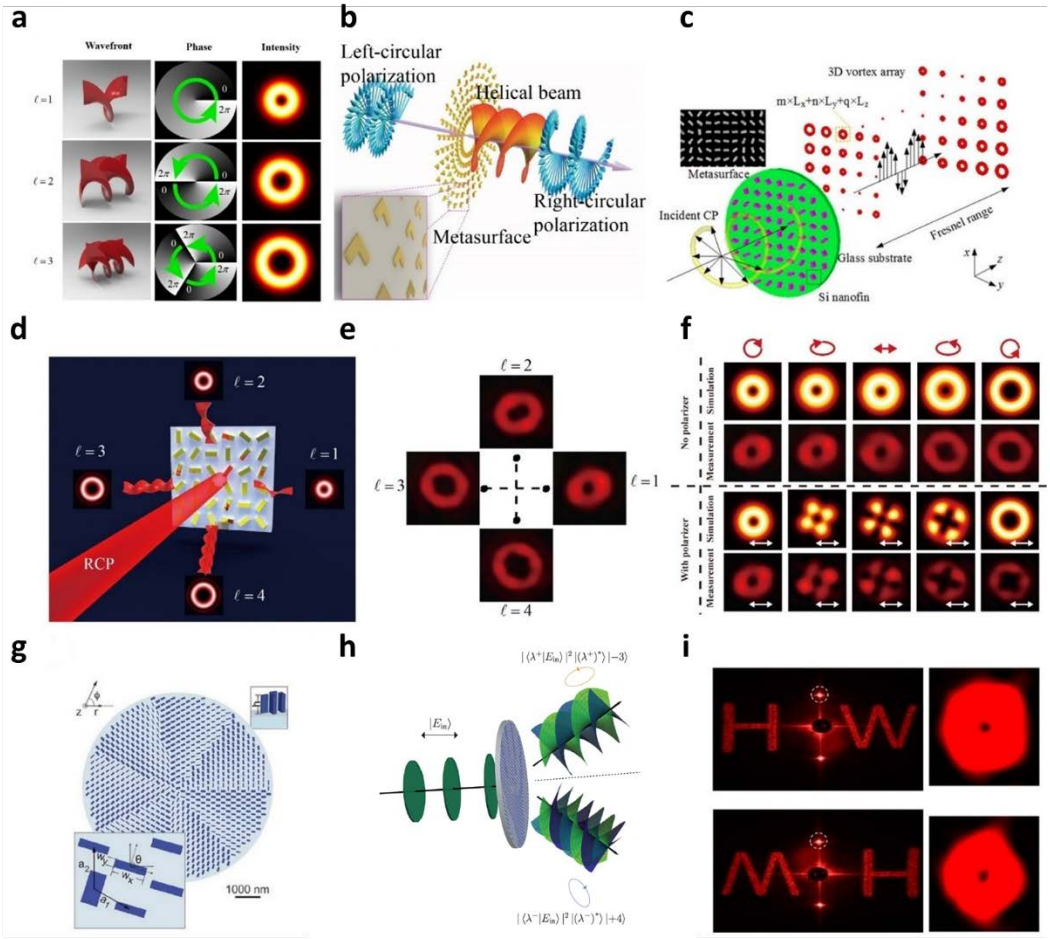

Figure 10. (a) The wavefront, phase and intensity profile of OAM beams with topological charges of $l=1$, $l=2$, and $l=3$. (b) Schematic of the OAM beam generation with a metasurface. The incident and scattered light is LCP and RCP, respectively, resulting an OAM beam with topological charge of $l=2$. (c) 3D vortex array generation by a dielectric

metasurface. The metasurface works within the Fresnel range. (d) Schematic of four OAM states from $l=1$ to $l=4$ generation under illumination of RCP light. (e) The experimentally observed intensity profiles of four OAM beams. (f) Simulated and experimentally recorded intensity profiles of the hybrid superposition of OAM modes $|R \quad l=1\rangle$ and $|L \quad l=-3\rangle$. (g) Schematic of dielectric metasurface consisting of nanopatterns with predesigned spatial variation of phase shifts and birefringence by adjusting the parameters including length, width and orientation angle. (h) Generation of two independent OAM states of *m*=-3 and *n*=-4 from two orthogonal SAM states with elliptical polarizations. The measured intensity profiles and interference pattern confirms that the two output beams (deflected by ±10°) contain the designed values of OAM. (i) The experimental results of holograms and vortex beams generated from a single metasurface device. Both the two holograms and the sign of two vortex beams ($l=1$ and $l=-1$) are dependent on the helicity of the incident beam. Figures reproduced with permission from: (a-b)[101b] Copyright2014, Nature Publishing Group; (c)[102] Copyright 2017, (i)[105] Copyright 2017, American Chemical Society; (d-f)[106] Copyright 2017, WILEY-VCH Verlag GmbH & Co. KGaA Weinheim; (g-h)[104] Copyright 2017, American Association for the Advancement of Science.

Light is characterized by amplitude, phase, and polarization. Besides phase, metasurface can also manipulate the polarization profile, which further expands its capabilities for various applications, such as vector beams[107] and vector vortex beams generation[108], image encoding[109]. Arbabi *et al.* demonstrated an dielectric metasurface approach to generate cylindrical vector beam by locally modifying the polarization[107e]. Radial and azimuthal vector beam were generated from *x* and *y* linearly polarized beam (**figure 11**a). Yue *et al.* reported a reflective-type plasmonic metasurface that can generate cylindrical vector vortex beams[108]. The vector vortex beams are obtained through the superposition of two circular components, which are the converted part with an additional phase pickup and the residual part without a

phase change (figure 11b). The ‘s’ pattern clearly verifies that the vector beam carries OAMs (figure 11c). Yue *et al*. also demonstrated an metasurface approach which can hide a high-resolution grayscale image into a laser beam with the spatially variant polarization states[109]. The encoded image can be revealed after passing through a linear polarizer (figure 11d). Metasurface platform provides a novel route to manipulate the polarization profile with high resolution, which renders this technology very attractive for diverse applications.

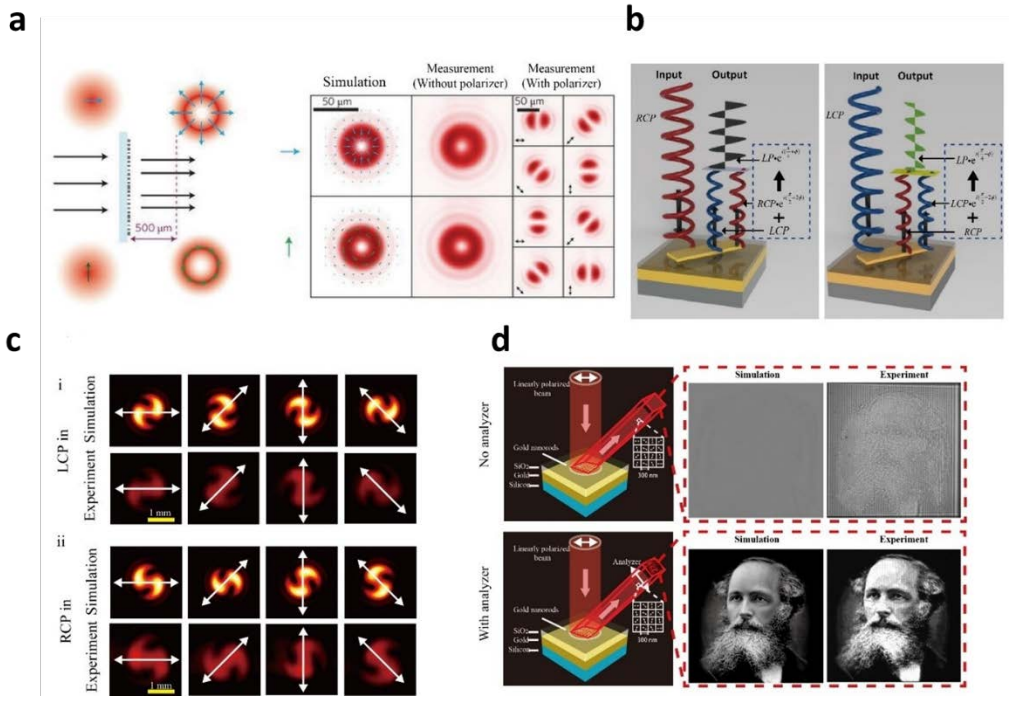

Figure 11 (a) Radially and azimuthally polarized light can be obtained by the same metasurface providing that the two incident light beams have orthogonal polarizations. (b) Illustration of polarization and phase evolution of emerging light on a single cell. For the LCP or RCP incident light, the emerging light is the superposition of the converted wave with an abrupt phase change (same handedness with that of incident beam) and non-converted wave (opposite handedness with that of incident beam), respectively. (c) Simulation and the experimental results of the vector vortex beam after passing through a polarizer (the white arrow shows the transmission direction of the polarizer). (d) Schematic for hiding a high-resolution grayscale

image. The image can be resolved by an analyzing polarizer. The four figures on the right side show the simulated and experimental results with and without analyzer. Figures reproduced with permission from: (a)[107e] Copyright 2015, (d)[109] Copyright 2018 Nature Publishing Group; (b-c)[108] Copyright 2016, American Chemical Society.

6. Geometric metasurface for nonlinear applications

The geometric metasurfaces introduced above are all within the scope of linear optics, i.e. the frequency of the scattered light carrying the geometric phase has the same frequency with the incident light. With the flourishing application of the plasmonic antennas in the field of optics, the analogue of the linear geometric phase in the nonlinear field has raised great attention. In the following, the nonlinear geometric phase and its application, along with the rotational Doppler effect will be introduced.

Under the illumination of the CP incident light, the co- or cross- polarized *n*th harmonic generation will have the nonlinear geometric phase of $(n\text{-}1)\sigma\theta$ or $(n+1)\sigma\theta$ [110], where $\sigma=\pm1$ represents the LCP(RCP) light and θ is the orientation of the nanoantenna. **Figure 12**a shows nanostructures with 2 and 4-fold rotational symmetry, the propagation direction of the third harmonic generation (THG) can be controlled by the nanoantenna distributions. Similarly, the geometric metasurface with highly nonlinear multi-quantum-well substrates can realize second harmonic generation (SHG) beam steering, focusing and polarization manipulation (figure 12b)[111].

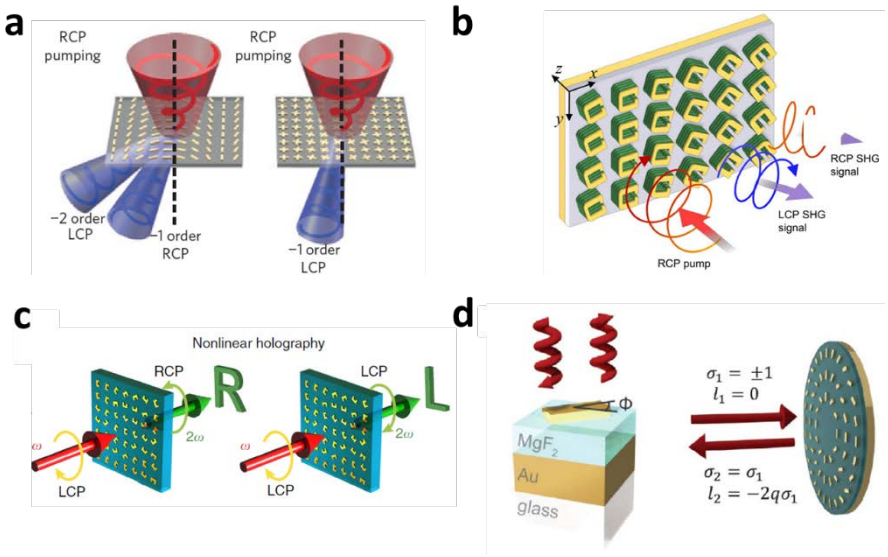

Figure 12. (a) Left: When the metasurface with two-fold rotational symmetry is under the RCP pumping, the RCP and LCP THG signals are diffracted to the -1 and -2 orders, respectively. Right: For the metasurface with four-fold rotational symmetry, the LCP THG signal is diffracted to the -1 order. (b) Under the RCP pump, LCP and RCP SHG signals are reflected to specific directions. (c) The holographic image generated by the SHG signal is related to its helicity. (d) Left: Schematic of a single antenna in the metasurface. Right: The helicity of the reflected light σ_2 is the same with that of the incident light σ_1, but the azimuthal phase number l_2 is changed to -2$q\sigma_1$ where q is related to the antenna distribution. Figures reproduced with permission from: (a)[110] Copyright 2015, (c)[112] Copyright 2016, Nature Publishing Group; (b)[111] Copyright 2015, American Physical Society; (d)[113] Copyright 2017, The Optical Society of America.

It is worth mentioning that the flexibility in controlling the nonlinear geometric phase has enabled the nonlinear holography and OAM generation. Using a metasurface with split ring antennas, the LCP incident light can generate three distinct images: the RCP image in the linear domain and the RCP, LCP images in the nonlinear domain (figure 12c)[112]. Walter et al. demonstrated a nonlinear metasurface hologram that can only reconstruct clear images by its

second harmonic generation, which can be used for image hiding[114]. Like the linear geometric phase, the positive or negative sign of the nonlinear geometric phase is determined by the helicity of the incident light. Thus the helicity-controlled OAM of light in harmonic generations can be realized[115]. If the chiral nanostructure is used, i.e. the field enhancement only occurs for a helicity, the high harmonic OAM can be generated using the linearly polarized incident light[116].

In contrast to the well-known translational Doppler effect, a rotating *q*-plate can shift the frequency of the converted light according to its rotation speed and direction, which is rotational Doppler effect[117]. Since geometric metasurface platform provides an efficient way for the generation of OAMs, rotational Doppler Effect is demonstrated using metasurface-based *q*-plate[113, 118]. In the linear domain, the *q*-plate imparts the OAM of $-2q\sigma_1$ to the converted light, where q is an integer determined by the antennas distribution and $\sigma_1=\pm1$ represents the helicity of the incident light. Hence the frequency shift equals to $2\Omega(q-1)\ \sigma_1$, and Ω is the angular rotation frequency of the object.

7. Other applications

Optical metasurfaces have revolutionized optical research in recent years, providing novel devices based on the geometric design and arrangement of light-scattering nano-antennas. Despite the various applications of the geometric metasurfaces mentioned above, a few other interesting applications are worth mentioning to inspire our readers in different fields.

(1) The combination of geometric phase and dynamic phase. Most of the reported metasurfaces are passive, meaning that the optical properties or functionalities are predefined once the components are fabricated and cannot be reconfigured dynamically. The two kinds of phases can be used together to achieve circular dichroism[119], or encode two independent phase functions to any kind of orthogonal polarizations[120].

(2) Complex amplitude control. Despite geometric metasurfaces only control the phase in most cases, an X-shaped metaatom with carefully controlled orientation angles of its two arms is reported to simultaneously control the amplitude and phase of the scattered light[121].

(3) A helicity preserving mirror. Generally, the helicity of the reflected light from the normal mirror is reversed, but the helicity can be preserved if the light shines on the high-efficiency reflective-type metasurface[122].

(4) Shared aperture antenna arrays. By interleaving of several independent antenna arrays, multiplexed geometric-phase profiles, as well as several independent functionalities can be achieved[123].

(5) THz modulators. Since the transmittance of THz waves through natural occurring materials is generally weak, the development of THz modulators is thereby hindered[124]. Benefiting from the strong interaction between the sub-wavelength metallic antennas and the THz waves, metasurfaces are very versatile in the THz wave applications[125], including the spectrum[126], polarization[127] and wavefront[128] modulation of the transmitted or reflected waves.

8. Conclusion and outlook

Metamaterials have brought up new ideas and enabled many ground-breaking discoveries due to the engineering flexibility in tailoring electromagnetic properties by introducing the meta-atom concept, but their practical applications in the optical range are primarily limited by the technical challenges such as three-dimensional (3D) nanofabrication. Amplitude, phase and polarization are the fundamental properties of light beam, which can be locally modified by using optical metasurfaces with planar structures, and it enables flat optical components with customer designed functionalities. Geometric optical metasurfaces have shown unprecedented capabilities in the manipulation of the polarization and phase of light at the subwavelength

scale, allowing for implementation of a wide variety of optical components. Some of the demonstrated unusual functionalities of metasurface devices cannot be obtained using even the highest quality commercial devices, and some have to be achieved using bulk optical components. The novel metasurface devices with designed functionalities render geometric metasurface devices very attractive for practical applications and might directly replace conventional optics in many applications

Active control of metasurfaces can further extend their applications by realizing tunable properties or switchable functionalities without actually replacing optical elements in a system[129]. Although thermal tuning[130], voltage bias[131], or geometrical deformation[132] have been incorporated into metasurfaces, this kind of tuning is based on functional materials (e.g., semiconductors and graphene). A key challenge in the field of optical metasurfaces is the realization of reconfigurable, random-access surfaces; devices whose individual nanostructures can be geometrically rearranged in order to produce 'on-demand' optical properties. Demonstration of this capability would unlock a variety of novel adaptive photonic devices[133], including dynamic lenses, active holograms, and functionality-switchable devices, and would have wide-ranging application in optics, data, communications and fundamental physics.

Acknowledgements

X.C. acknowledges the Engineering and Physical Sciences Research Council of the United Kingdom (Grant Ref: EP/ P029892/1).

References

[1] a) N. Yu, F. Capasso, *Nat. Mater.* **2014**, *13*, 139; b) X. J. Ni, N. K. Emani, A. V. Kildishev, A. Boltasseva, V. M. Shalaev, *Science* **2012**, *335*, 427.

[2] C. Wenshan, *Optical Metamaterials*, Springer, London, **2010.**

[3] a) J. B. Pendry, *Phys. Rev. Lett.* **2000**, *85*, 3966; b) N. Fang, H. Lee, C. Sun, X. Zhang, *Science* **2005**, *308*, 534; c) R. A. Shelby, D. R. Smith, S. Schultz, *Science* **2001**, *292*, 77; d) V. G. Veselago, *Phys. Usp.* **1968**, *10*, 509.

[4] a) N. F. Yu, P. Genevet, M. A. Kats, F. Aieta, J. P. Tetienne, F. Capasso, Z. Gaburro, *Science* **2011**, *334*, 333; b) Y. Zhao, A. Alù, *Nano Lett.* **2013**, *13*, 1086; c) A. Pors, S. I. Bozhevolnyi, *Opt. Express* **2013**, *21*, 27438.

[5] a) S. Pancharatnam, presented at Proceedings of the Indian Academy of Sciences-Section A **1956**; b) M. V. Berry, presented at Proceedings of the Royal Society of London A: Mathematical, Physical and Engineering Sciences **1984**; c) Z. e. Bomzon, G. Biener, V. Kleiner, E. Hasman, *Opt. Lett.***2002**, *27*, 1141; d) E. Hasman, V. Kleiner, G. Biener, A. Niv, *Appl. Phys. Lett.* **2003**, *82*, 328.

[6] F. Aieta, P. Genevet, N. F. Yu, M. A. Kats, Z. Gaburro, F. Capasso, *Nano Lett.* **2012**, *12*, 1702.

[7] L. Huang, X. Chen, H. Mühlenbernd, G. Li, B. Bai, Q. Tan, G. Jin, T. Zentgraf, S. Zhang, *Nano Lett.* **2012**, *12*, 5750.

[8] G. Zheng, H. Mühlenbernd, M. Kenney, G. Li, T. Zentgraf, S. Zhang, *Nat. Nanotechnol.* **2015**, *10*, 308.

[9] X. Chen, L. Huang, H. Muhlenbernd, G. Li, B. Bai, Q. Tan, G. Jin, C. W. Qiu, S. Zhang, T. Zentgraf, *Nat. Commun.* **2012**, *3*, 1198.

[10] X. Chen, L. Huang, H. Mühlenbernd, G. Li, B. Bai, Q. Tan, G. Jin, C.-W. Qiu, T. Zentgraf, S. Zhang, *Adv. Opt. Mater.* **2013**, *1*, 517.

[11] X. Chen, M. Chen, M. Q. Mehmood, D. Wen, F. Yue, C.-W. Qiu, S. Zhang, *Adv. Opt. Mater.* **2015**, *3*, 1201.

[12] M. Kang, T. Feng, H.-T. Wang, J. Li, *Opt. Express* **2012**, *20*, 15882.

[13] D. Wen, F. Yue, M. Ardron, X. Chen, *Sci. Rep.* **2016**, *6*, 27628.

[14] D. Wen, S. Chen, F. Yue, K. Chan, M. Chen, M. Ardron, K. F. Li, P. W. H. Wong, K. W. Cheah, E. Y. B. Pun, G. Li, S. Zhang, X. Chen, *Adv. Opt. Mater.* **2016**, *4*, 321.

[15] M. Khorasaninejad, W. Chen, A. Zhu, J. Oh, R. Devlin, D. Rousso, F. Capasso, *Nano Lett.* **2016**, *16*, 4595.

[16] H. S. Ee, R. Agarwal, *Nano Lett.* **2016**, *16*, 2818.

[17] X. Yin, T. Steinle, L. Huang, T. Taubner, M. Wuttig, T. Zentgraf, H. Giessen, *Light Sci. Appl.* **2017**, *6*, e17016.

[18] a) R. Z. Li, Z. Y. Guo, W. Wang, J. R. Zhang, K. Y. Zhou, J. L. Liu, S. L. Qu, S. T. Liu, J. Gao, *Photonics Research* **2015**, *3*, 252; b) X. Chen, Y. Zhang, L. Huang, S. Zhang, *Adv. Opt. Mater.* **2014**, *2*, 978.

[19] Y. Bao, Q. Jiang, Y. Kang, X. Zhu, Z. Fang, *Light Sci. Appl.* **2017**, *6*, e17071.

[20] Z. Zhao, M. Pu, H. Gao, J. Jin, X. Li, X. Ma, Y. Wang, P. Gao, X. Luo, *Sci. Rep.* **2015**, *5,* 15781.

[21] K. Li, Y. Guo, M. Pu, X. Li, X. Ma, Z. Zhao, X. Luo, *Opt. Express* **2017**, *25*, 21419.

[22] a) W. T. Chen, A. Y. Zhu, V. Sanjeev, M. Khorasaninejad, Z. Shi, E. Lee, F. Capasso, *arXiv preprint arXiv:1711.09343* **2017**; b) S. Wang, P. C. Wu, V.-C. Su, Y.-C. Lai, C. H. Chu, J.-W. Chen, S.-H. Lu, J. Chen, B. Xu, C.-H. Kuan, *Nat. Commun.* **2017**, *8*, 187.

[23] W. Luo, S. Xiao, Q. He, S. Sun, L. Zhou, *Adv. Opt. Mater.* **2015**, *3*, 1102.

[24] M. Khorasaninejad, W. T. Chen, R. C. Devlin, J. Oh, A. Y. Zhu, F. Capasso, *Science* **2016**, *352*, 1190.

[25] W. T. Chen, A. Y. Zhu, M. Khorasaninejad, Z. Shi, V. Sanjeev, F. Capasso, *Nano Lett.* **2017**, *17*, 3188.

[26] a) M. Khorasaninejad, W. Chen, J. Oh, F. Capasso, *Nano Lett.* **2016**, *16*, 3732; b) A. Y. Zhu, W.-T. Chen, M. Khorasaninejad, J. Oh, A. Zaidi, I. Mishra, R. C. Devlin, F. Capasso, *APL Photonics* **2017**, *2*, 036103.

[27] B. H. Chen, P. C. Wu, V. C. Su, Y. C. Lai, C. H. Chu, I. C. Lee, J. W. Chen, Y. H. Chen, Y. C. Lan, C. H. Kuan, D. P. Tsai, *Nano Lett.* **2017**, *17*, 6345.

[28] G. X. Zheng, W. B. A. Wu, Z. L. Li, S. Zhang, M. Q. Mehmood, P. A. He, S. Li, *Opt. Lett.***2017**, *42*, 1261.

[29] D. Lin, P. Fan, E. Hasman, M. L. Brongersma, *Science* **2014**, *345*, 298.

[30] D. Lin, A. L. Holsteen, E. Maguid, G. Wetzstein, P. G. Kik, E. Hasman, M. L. Brongersma, *Nano Lett.* **2016**, *16*, 7671.

[31] Q. Fan, P. Huo, D. Wang, Y. Liang, F. Yan, T. Xu, *Sci. Rep.* **2017**, *7*, 45044.

[32] R. Z. Li, F. Shen, Y. X. Sun, W. Wang, L. Zhu, Z. Y. Guo, *J Phys D Appl Phys.* **2016**, *49,* 145101.

[33] Z. Li, I. Kim, L. Zhang, M. Q. Mehmood, M. S. Anwar, M. Saleem, D. Lee, K. T. Nam, S. Zhang, B. Luk'yanchuk, *ACS Nano* **2017**, *11*, 9382.

[34] D. D. Wen, F. Y. Yue, G. X. Li, G. X. Zheng, K. L. Chan, S. M. Chen, M. Chen, K. F. Li, P. W. H. Wong, K. W. Cheah, E. Y. B. Pun, S. Zhang, X. Z. Chen, *Nat. Commun.* **2015**, *6,* 8241.

[35] F. Y. Yue, X. F. Zang, D. D. Wen, Z. L. Li, C. M. Zhang, H. G. Liu, B. D. Gerardot, W. Wang, G. X. Zheng, X. Z. Chen, *Sci. Rep.* **2017**, *7,* 11440.

[36] J. Burch, D. D. Wen, X. Z. Chen, A. Di Falco, *Sci. Rep.* **2017**, *7,* 4520.

[37] X. Li, L. Chen, Y. Li, X. Zhang, M. Pu, Z. Zhao, X. Ma, Y. Wang, M. Hong, X. Luo, *Sci. Adv.* **2016**, *2,* e1601102.

[38] W. Wan, J. Gao, X. Yang, *ACS Nano* **2016**, *10*, 10671.

[39] B. Wang, F. Dong, Q. T. Li, D. Yang, C. Sun, J. Chen, Z. Song, L. Xu, W. Chu, Y. F. Xiao, Q. Gong, Y. Li, *Nano Lett.* **2016**, *16*, 5235.

[40] W. Zhao, B. Liu, H. Jiang, J. Song, Y. Pei, Y. Jiang, *Opt. Lett.* **2016**, *41*, 147.

[41] J. Upatnieks, J. Marks, R. Fedorowicz, *Appl. Phys. Lett.* **1966**, *8*, 286.

[42] a) S. Choudhury, U. Guler, A. Shaltout, V. M. Shalaev, A. V. Kildishev, A. Boltasseva, *Adv. Opt. Mater.* **2017**, *5,* 1700196; b) R. C. Devlin, M. Khorasaninejad, W. T. Chen, J. Oh, F. Capasso, *Proc. Natl. Acad. Sci. USA* **2016**, *113*, 10473; c) M. Khorasaninejad, A. Ambrosio, P. Kanhaiya, F. Capasso, *Sci. Adv.* **2016**, *2*, e1501258.

[43] B. Wang, F. Dong, D. Yang, Z. Song, L. Xu, W. Chu, Q. Gong, Y. Li, *Optica* **2017**, *4*, 1368.

[44] L. Huang, X. Chen, H. Mühlenbernd, H. Zhang, S. Chen, B. Bai, Q. Tan, G. Jin, K.-W. Cheah, C.-W. Qiu, *Nat. Commun.* **2013**, *4*, 2808.

[45] K. Huang, Z. Dong, S. Mei, L. Zhang, Y. Liu, H. Liu, H. Zhu, J. Teng, B. Luk'yanchuk, J. K. Yang, *Laser Photonics Rev.* **2016**, *10*, 500.

[46] Q. Wei, L. Huang, X. Li, J. Liu, Y. Wang, *Adv. Opt. Mater.* **2017**, *5,* 18.

[47] S. C. Malek, H. S. Ee, R. Agarwal, *Nano Lett.* **2017**, *17*, 3641.

[48] L. Huang, H. Mühlenbernd, X. Li, X. Song, B. Bai, Y. Wang, T. Zentgraf, *Adv. Mater.* **2015**, *27*, 6444.

[49] W. T. Chen, M. Khorasaninejad, A. Y. Zhu, J. Oh, R. C. Devlin, A. Zaidi, F. Capasso, *Light Sci. Appl.* **2017**, *6,* e16259.

[50] X. Li, M. Pu, Z. Zhao, X. Ma, J. Jin, Y. Wang, P. Gao, X. Luo, *Sci. Rep.* **2016**, *6,* 20524.

[51] Q. B. Fan, D. P. Wang, P. C. Huo, Z. J. Zhang, Y. Z. Liang, T. Xu, *Opt. Express* **2017**, *25*, 9285.

[52] J. Zhou, Y. Liu, Y. Ke, H. Luo, S. Wen, *Opt. Lett.***2015**, *40*, 3193.

[53] Z. Li, H. Cheng, Z. Liu, S. Chen, J. Tian, *Adv. Opt. Mater.* **2016**, *4*, 1230.

[54] K. Y. Bliokh, F. Rodríguez-Fortuño, F. Nori, A. V. Zayats, *Nat. Photonics* **2015**, *9*, 796.

[55] Z. C. Liu, Z. C. Li, Z. Liu, J. X. Li, H. Cheng, P. Yu, W. W. Liu, C. C. Tang, C. Z. Gu, J. J. Li, S. Q. Chen, J. G. Tian, *Adv. Funct. Mater.* **2015**, *25*, 5428.

[56] J. Liu, Z. Li, W. Liu, H. Cheng, S. Chen, J. Tian, *Adv. Opt. Mater.* **2016**, *4*, 2028.

[57] D. Wen, F. Yue, S. Kumar, Y. Ma, M. Chen, X. Ren, P. E. Kremer, B. D. Gerardot, M. R. Taghizadeh, G. S. Buller, X. Chen, *Opt. Express* **2015**, *23*, 10272.

[58] M. Khorasaninejad, K. B. Crozier, *Nat. Commun.* **2014**, *5*, 5386.

[59] Z. Li, W. Liu, H. Cheng, J. Liu, S. Chen, J. Tian, *Sci. Rep.* **2016**, *6*, 35485.

[60] a) Y. Ke, Y. Liu, Y. He, J. Zhou, H. Luo, S. Wen, *Appl. Phys. Lett.* **2015**, *107*, 041107; b) X. Ling, X. Zhou, X. Yi, W. Shu, Y. Liu, S. Chen, H. Luo, S. Wen, D. Fan, *Light Sci. Appl.* **2015**, *4*, e290; c) Y. Liu, X. Ling, X. Yi, X. Zhou, S. Chen, Y. Ke, H. Luo, S. Wen, *Opt. Lett.***2015**, *40*, 756.

[61] W. J. Luo, S. L. Sun, H. X. Xu, Q. He, L. Zhou, *Phys. Rev. Appl.* **2017**, *7,* 044033.

[62] Z. Li, W. Liu, H. Cheng, S. Chen, J. Tian, *Adv. Opt. Mater.* **2017**, *5*, 1700413.

[63] X. Hu, L. Wen, S. Song, Q. Chen, *Nanotechnology* **2015**, *26*, 505203.

[64] X. Luo, M. Pu, X. Li, X. Ma, *Light Sci. Appl.* **2017**, *6*, e16276.

[65] B. Wang, F. Dong, H. Feng, D. Yang, Z. Song, L. Xu, W. Chu, Q. Gong, Y. Li, *ACS Photonics* **2017**. DOI: 10.1021/acsphotonics.7b01191.

[66] a) P. C. Wu, J.-W. Chen, C.-W. Yin, Y.-C. Lai, T. L. Chung, C. Y. Liao, B. H. Chen, K.-W. Lee, C.-J. Chuang, C.-M. Wang, D. P. Tsai, *ACS Photonics* **2017**, DOI: 10.1021/acsphotonics.7b01527; b) A. Pors, M. G. Nielsen, S. I. Bozhevolnyi, *Optica* **2015**, *2*, 716; c) A. Pors, S. I. Bozhevolnyi, *Phys. Rev. Appl.* **2016**, *5*, 064015; d) F. Ding, A. Pors, Y. Chen, V. A. Zenin, S. I. Bozhevolnyi, *ACS Photonics* **2017**, *4*, 943; e) W. T. Chen, P. Torok, M. R. Foreman, C. Y. Liao, W. Y. Tsai, P. R. Wu, D. P. Tsai, *Nanotechnology* **2016**, *27,* 224002.

[67] A. Shaltout, J. Liu, A. Kildishev, V. Shalaev, *Optica* **2015**, *2,* 860.

[68] J. Zhou, H. Qian, G. Hu, H. Luo, S. Wen, Z. Liu, *ACS Nano* **2017**, *12,* 82.

[69] S. Wang, X. Wang, Q. Kan, J. Ye, S. Feng, W. Sun, P. Han, S. Qu, Y. Zhang, *Opt. Express* **2015**, *23*, 26434.

[70] H. Cheng, Z. Liu, S. Chen, J. Tian, *Adv. Mater.* **2015**, *27*, 5410.

[71] P. Yu, J. Li, C. Tang, H. Cheng, Z. Liu, Z. Li, Z. Liu, C. Gu, J. Li, S. Chen, *Light Sci. Appl.* **2016**, *5*, e16096.

[72] a) N. K. Grady, J. E. Heyes, D. R. Chowdhury, Y. Zeng, M. T. Reiten, A. K. Azad, A. J. Taylor, D. A. Dalvit, H.-T. Chen, *Science* **2013**, *340,* 1235399; b) Z. Li, W. Liu, H. Cheng, S. Chen, J. Tian, *Sci. Rep.* **2017**, *7*, 8204.

[73] a) J. Li, P. Yu, C. Tang, H. Cheng, J. Li, S. Chen, J. Tian, *Adv. Opt. Mater.* **2017**, *5,* 1700152; b) J. Li, S. Chen, H. Yang, J. Li, P. Yu, H. Cheng, C. Gu, H. T. Chen, J. Tian, *Adv. Funct. Mater.* **2015**, *25*, 704.

[74] B. Xie, K. Tang, H. Cheng, Z. Liu, S. Chen, J. Tian, *Adv. Mater.* **2017**, *29,* 1603507.

[75] B. Xie, H. Cheng, K. Tang, Z. Liu, S. Chen, J. Tian, *Phys. Rev. Appl.* **2017**, *7*, 024010.

[76] Z. Liu, S. Chen, J. Li, H. Cheng, Z. Li, W. Liu, P. Yu, J. Xia, J. Tian, *Opt. Lett.***2014**, *39*, 6763.

[77] Z. Liu, S. Chen, H. Cheng, Z. Li, W. Liu, J. Tian, *Plasmonics* **2016**, *11*, 353.

[78] L. Ju, B. Geng, J. Horng, C. Girit, M. Martin, Z. Hao, H. A. Bechtel, X. Liang, A. Zettl, Y. R. Shen, *Nat. Nanotechnol.* **2011**, *6*, 630.

[79] H. Cheng, S. Chen, P. Yu, W. Liu, Z. Li, J. Li, B. Xie, J. Tian, *Adv. Opt. Mater.* **2015**, *3*, 1744.

[80] C. Wang, W. Liu, Z. Li, H. Cheng, Z. Li, S. Chen, J. Tian, *Adv. Opt. Mater.* **2018**, *6,* 1701047.

[81] a) L. Huang, X. Chen, B. Bai, Q. Tan, G. Jin, T. Zentgraf, S. Zhang, *Light Sci. Appl.* **2013**, *2,* e20; b) N. Shitrit, S. Maayani, D. Veksler, V. Kleiner, E. Hasman, *Opt. Lett.***2013**, *38*, 4358.

[82] S. Xiao, F. Zhong, H. Liu, S. Zhu, J. Li, *Nat. Commun.* **2015**, *6*, 8360.

[83] J. Lin, J. P. B. Mueller, Q. Wang, G. H. Yuan, N. Antoniou, X. C. Yuan, F. Capasso, *Science* **2013**, *340*, 331.

[84] P. Genevet, D. Wintz, A. Ambrosio, A. She, R. Blanchard, F. Capasso, *Nat. Nanotechnol.* **2015**, *10*, 804.

[85] B. Zhu, G. Ren, Y. Gao, B. Wu, C. Wan, S. Jian, *Opt. Express* **2015**, *23*, 32420.

[86] G. Spektor, A. David, B. Gjonaj, G. Bartal, M. Orenstein, *Nano Lett.* **2015**, *15*, 5739.

[87] J. Li, P. Tang, W. Liu, T. Huang, J. Wang, Y. Wang, F. Lin, Z. Fang, X. Zhu, *Appl. Phys. Lett.* **2015**, *106*, 161106.

[88] Q. Tan, Q. Guo, H. Liu, X. Huang, S. Zhang, *Nanoscale* **2017**, *9*, 4944.

[89] Q. Xu, X. Zhang, Y. Xu, C. Ouyang, Z. Tian, J. Gu, J. Li, S. Zhang, J. Han, W. Zhang, *Laser Photonics Rev.* **2017**, *11,* 1600212.

[90] A. I. Rusanov, A. G. Nekrasov, *Langmuir* **2010**, *26*, 13767.

[91] Y. He, B. Wang, R. Dukor, L. Nafie, *Planta Med.* **2012**, *78*, CL45.
[92] a) J. K. Gansel, M. Thiel, M. S. Rill, M. Decker, K. Bade, V. Saile, G. von Freymann, S. Linden, M. Wegener, *Science* **2009**, *325*, 1513; b) S. Zhang, Y.-S. Park, J. Li, X. Lu, W. Zhang, X. Zhang, *Phys. Rev. Lett.* **2009**, *102*, 023901.
[93] A. Papakostas, A. Potts, D. Bagnall, S. Prosvirnin, H. Coles, N. Zheludev, *Phys. Rev. Lett.* **2003**, *90*, 107404.
[94] A. Shaltout, J. Liu, V. M. Shalaev, A. V. Kildishev, *Nano Lett.* **2014**, *14*, 4426.
[95] Z. Liu, Z. Li, Z. Liu, H. Cheng, W. Liu, C. Tang, C. Gu, J. Li, H.-T. Chen, S. Chen, *ACS Photonics* **2017**, *4*, 2061.
[96] D. D. Wen, F. Y. Yue, C. M. Zhang, X. F. Zang, H. G. Liu, W. Wang, X. Z. Chen, *Appl. Phys. Lett.* **2017**, *111,* 023102.
[97] Z. Y. Liu, Q. J. Wang, L. R. Yuan, Y. Y. Zhu, *J Phys D Appl Phys.* **2017**, *50,* 245103.
[98] P. C. Wu, W.-Y. Tsai, W. T. Chen, Y.-W. Huang, T.-Y. Chen, J.-W. Chen, C. Y. Liao, C. H. Chu, G. Sun, D. P. Tsai, *Nano Lett.* **2016**, *17*, 445.
[99] Q. Guo, C. Schlickriede, D. Wang, H. Liu, Y. Xiang, T. Zentgraf, S. Zhang, *Opt. Express* **2017**, *25*, 14300.
[100] a) F. Cardano, E. Karimi, S. Slussarenko, L. Marrucci, C. de Lisio, E. Santamato, *Appl. Opt.* **2012**, *51*, C1; b) Y. S. Rumala, G. Milione, T. A. Nguyen, S. Pratavieira, Z. Hossain, D. Nolan, S. Slussarenko, E. Karimi, L. Marrucci, R. R. Alfano, *Opt. Lett.* **2013**, *38*, 5083; c) M. Beresna, M. Gecevičius, P. G. Kazansky, T. Gertus, *Appl. Phys. Lett.* **2011**, *98*, 201101.
[101] a) M. Kang, J. Chen, X. L. Wang, H. T. Wang, *J. Opt. Soc. Am.* **2012**, *29*, 572; b) E. Karimi, S. A. Schulz, I. De Leon, H. Qassim, J. Upham, R. W. Boyd, *Light Sci. Appl.* **2014**, *3*, e167; c) L. Huang, X. Chen, H. Muhlenbernd, G. Li, B. Bai, Q. Tan, G. Jin, T. Zentgraf, S. Zhang, *Nano Lett.* **2012**, *12*, 5750; d) Y. M. Yang, W. Y. Wang, P. Moitra, I. I. Kravchenko, D. P. Briggs, J. Valentine, *Nano Lett.* **2014**, *14*, 1394; e) P. Chen, S.-J. Ge, W. Duan, B.-Y. Wei, G.-X. Cui, W. Hu, Y.-Q. Lu, *ACS Photonics* **2017**, *4,* 1333; f) R. C. Devlin, A. Ambrosio, D. Wintz, S. L. Oscurato, A. Y. Zhu, M. Khorasaninejad, J. Oh, P. Maddalena, F. Capasso, *Opt. Express* **2017**, *25*, 377.
[102] L. Huang, X. Song, B. Reineke, T. Li, X. Li, J. Liu, S. Zhang, Y. Wang, T. Zentgraf, *ACS Photonics* **2017**, *4*, 338.
[103] F. Yue, D. Wen, C. Zhang, B. D. Gerardot, W. Wang, S. Zhang, X. Chen, *Adv. Mater.* **2017**, *29*, 1603838.
[104] R. C. Devlin, A. Ambrosio, N. A. Rubin, J. B. Mueller, F. Capasso, *Science* **2017**, *358*, 896.
[105] C. Zhang, F. Yue, D. Wen, M. Chen, Z. Zhang, W. Wang, X. Chen, *ACS Photonics* **2017**, *4*, 1906.
[106] F. Y. Yue, D. D. Wen, C. M. Zhang, B. D. Gerardot, W. Wang, S. Zhang, X. Z. Chen, *Adv. Mater.* **2017**, *29,* 1603838.
[107] a) H. Chen, Z. Chen, Q. Li, H. Lv, Q. Yu, X. Yi, *J. Mod. Opt.* **2015**, *62*, 638; b) H. Chen, X. Ling, Q. Li, H. Lv, H. Yu, X. Yi, *Optik* **2017**, *134*, 227; c) J. Zhou, W. Zhang, Y. Liu, Y. Ke, Y. Liu, H. Luo, S. Wen, *Sci. Rep.* **2016**, *6,* 34276; d) X. N. Yi, X. H. Ling, Z. Y. Zhang, Y. Li, X. X. Zhou, Y. C. Liu, S. Z. Chen, H. L. Luo, S. C. Wen, *Opt. Express* **2014**, *22*, 17207; e) A. Arbabi, Y. Horie, M. Bagheri, A. Faraon, *Nat. Nanotechnol.* **2015**, *10*, 937.
[108] F. Yue, D. Wen, J. Xin, B. D. Gerardot, J. Li, X. Chen, *ACS photonics* **2016**, *3*, 1558.
[109] F. Yue, C. Zhang, X. Zang, D. Wen, B. D. Gerardot, S. Zhang, X. Chen, Light Sci. Appl. **2018**, *7*, 17129.
[110] G. Li, S. Chen, N. Pholchai, B. Reineke, P. W. H. Wong, E. Y. B. Pun, K. W. Cheah, T. Zentgraf, S. Zhang, *Nat. Mater.* **2015**, *14*, 607.
[111] M. Tymchenko, J. S. Gomez-Diaz, J. Lee, N. Nookala, M. A. Belkin, A. Alù, *Phys. Rev. Lett.* **2015**, *115*, 207403.
[112] W. Ye, F. Zeuner, X. Li, B. Reineke, S. He, C.-W. Qiu, J. Liu, Y. Wang, S. Zhang, T. Zentgraf, *Nat. Commun.* **2016**, *7,* 11930.
[113] P. Georgi, C. Schlickriede, G. X. Li, S. Zhang, T. Zentgraf, *Optica* **2017**, *4*, 1000.
[114] F. Walter, G. Li, C. Meier, S. Zhang, T. Zentgraf, *Nano Lett.* **2017**, *17*, 3171.

[115] a) M. Tymchenko, J. Gomez-Diaz, J. Lee, N. Nookala, M. Belkin, A. Alù, *Phys. Rev. B* **2016**, *94*, 214303; b) G. Li, L. Wu, K. F. Li, S. Chen, C. Schlickriede, Z. Xu, S. Huang, W.-D. Li, Y. J. Liu, E. Y.-B. Pun, *Nano Lett.* **2017**, *17*, 7974.
[116] A. Cala'Lesina, P. Berini, L. Ramunno, *Opt. Express* **2017**, *25*, 2569.
[117] J. Poynting, *Proceedings of the Royal Society of London. Series A, Containing Papers of a Mathematical and Physical Character* **1909**, *82*, 560.
[118] a) G. Li, T. Zentgraf, S. Zhang, *Nature Physics* **2016**, *12*, 736; b) G. Li, S. Zhang, T. Zentgraf, *Nat. Rev. Mater.* **2017**, *2*, 17010.
[119] M. Kenney, S. Li, X. Zhang, X. Su, T. T. Kim, D. Wang, D. Wu, C. Ouyang, J. Han, W. Zhang, *Adv. Mater.* **2016**, *28*, 9567.
[120] J. P. Balthasar Mueller, N. A. Rubin, R. C. Devlin, B. Groever, F. Capasso, *Phys. Rev. Lett.* **2017**, *118*, 113901.
[121] G.-Y. Lee, G. Yoon, S.-Y. Lee, H. Yun, J. Cho, K. Lee, H. Kim, J. Rho, B. Lee, *arXiv preprint arXiv:1706.09632* **2017**.
[122] S. Xiao, H. Mühlenbernd, G. Li, M. Kenney, F. Liu, T. Zentgraf, S. Zhang, J. Li, *Adv. Opt. Mater.* **2016**, *4*, 654.
[123] a) E. Maguid, I. Yulevich, D. Veksler, V. Kleiner, M. L. Brongersma, E. Hasman, *Science* **2016**, aaf3417; b) E. Maguid, I. Yulevich, M. Yannai, V. Kleiner, M. L. Brongersma, E. Hasman, *Light Sci. Appl.* **2017**, *6*, e17027.
[124] J. W. He, J. S. Ye, X. K. Wang, Q. Kan, Y. Zhang, *Sci. Rep.* **2016**, *6,* 6:28800.
[125] a) J. He, Y. Zhang, *J. Phys. D* **2017**, *50*, 464004; b) J. Y. Guo, X. K. Wang, J. W. He, H. Zhao, S. F. Feng, P. Han, J. S. Ye, W. F. Sun, G. H. Situ, Y. Zhang, *Adv. Opt. Mater.* **2018**, *6,* 1700925; c) H. Zhao, X. K. Wang, J. W. He, J. Y. Guo, J. S. Ye, Q. Kan, Y. Zhang, *Sci. Rep.* **2017**, *7,* 17882.
[126] J. W. He, Z. W. Xie, W. F. Sun, X. K. Wang, Y. D. Ji, S. Wang, Y. Lin, Y. Zhang, *Plasmonics* **2016**, *11*, 1285.
[127] L. Cong, N. Xu, J. Han, W. Zhang, R. Singh, *Adv. Mater.* **2015**, *27*, 6630.
[128] A. Minasyan, C. Trovato, J. Degert, E. Freysz, E. Brasselet, E. Abraham, *Opt. Lett.* **2017**, *42*, 41.
[129] C. H. Chu, M. L. Tseng, J. Chen, P. C. Wu, Y. H. Chen, H. C. Wang, T. Y. Chen, W. T. Hsieh, H. J. Wu, G. Sun, *Laser Photonics Rev.* **2016**, *10*, 986.
[130] M. A. Kats, D. Sharma, J. Lin, P. Genevet, R. Blanchard, Z. Yang, M. M. Qazilbash, D. N. Basov, S. Ramanathan, F. Capasso, *Appl. Phys. Lett.* **2012**, *101*, 221101.
[131] a) Y. Yao, R. Shankar, M. A. Kats, Y. Song, J. Kong, M. Loncar, F. Capasso, *Nano Lett.* **2014**, *14*, 6526; b) P. C. Wu, N. Papasimakis, D. P. Tsai, *Phys. Rev. Appl.* **2016**, *6*, 044019.
[132] a) H.-S. Ee, R. Agarwal, *Nano Lett.* **2016**, *16*, 2818; b) M. L. Tseng, J. Yang, M. Semmlinger, C. Zhang, P. Nordlander, N. J. Halas, *Nano Lett.* **2017**, *17*, 6034.
[133] P. C. Wu, W. Zhu, Z. X. Shen, P. H. J. Chong, W. Ser, D. P. Tsai, A. Q. Liu, *Adv. Opt. Mater.* **2017**, *5,* 1600938.